Supporting Information

Cascade Mechanochemical Transformation of a Benzobarrelane Polymer: A Neighboring Repeat Unit Effect

Daniel C. Lee,[1‡] Rui Xu,[1,2,3‡] Erica J. Flear,[1‡] Ke Zheng,[1] Søren Holm,[1,2] Diptarka Hait,[1,2] Todd J. Martínez,[1,2*] and Yan Xia[1*]

[1]Department of Chemistry, Stanford University, Stanford, California 94305, United States

[3]Stanford PULSE Institute, SLAC National Accelerator Laboratory, Menlo Park, California 94025, United States

[3]Department of Aerospace and Mechanical Engineering, University of Southern California, Los Angeles, California 90089, United States

S1. Materials and methods....2

S2. Synthetic Procedures....3

S3. Design of reference compounds representing mechanochemically ring-opened repeat unit structures. .13

S4. Calculation of mechanoactivation percentage based on NMR analysis. 15

S5. Control polymers....16

S5.1. Synthetic procedure for poly1-H_2 and its attempted mechanoactivation. 16

S6. Computational details....20

S7. Movie files of AISMD simulations 42

S1. Materials and methods

All reagents were obtained from commercial vendors and used as received unless otherwise noted.

Flash column chromatography was performed using F60 silica gel (40-63 μm, 230-400 mesh, 60Å) purchased from Silicycle. Analytical thin-layer chromatography (TLC) was carried out on 250 μm 60-F254 silica gel plates purchased from EMD Millipore, and visualization was effected by observation of fluorescence-quenching with ultraviolet light and staining with either panisaldehyde or potassium permanganate as a developing agent.

^{1}H NMR and ^{13}C NMR spectra were recorded on Varian Inova 600, Varian Inova 500, Varian Mercury 400, or Varian Inova 300 spectrometers operating respectively at 600, 500, 400, and 300 MHz for 1H and at 150, 125, 100, and 75 MHz for ^{13}C. Chemical shifts are reported in parts per million (ppm) relative to residual protonated solvent for ^{1}H ($CHCl_3$ = δ 7.26) and relative to carbon resonances of the solvent for ^{13}C ($CDCl_3$ = δ 77.0). Peak multiplicities are annotated as follows: app = apparent, br = broad, s = singlet, d = doublet, t = triplet, q = quartet, p = quintet, m = multiplet.

Gel permeation chromatography (GPC) was carried out in THF on two PolyPore columns (Agilent) connected in series with a DAWN multiangle laser light scattering (MALLS) detector and an Optilab TrEX differential refractometer (both from Wyatt Technology). dn/dc values were obtained for each injection by assuming 100% mass elution from the columns.

Ultrasonication was performed in a 10 mL ultrasonic vessel (Ace Glass 9843-25) with a Branson 450 sonifier equipped with a 1/8'' (3 mm diameter) tapered microtip. The distance between the tip and bottom of the vessel was 1 cm. The vessel was connected to the horn with a bushing and an O-ring to ensure airtightness. The power was calibrated according to reported procedures (37). Sonication was performed using pulsed ultrasound (1.0 s on, 1.0 s off) at 20 kHz under Ar with an output of 9.2 W/cm^2. The vessel was placed in an ice bath to maintain a temperature inside the vessel of 6–9 ºC throughout sonication. Sonication time in this manuscript all refers to on-time.

S2. Synthetic Procedures

S2.1. Synthetic procedures for compounds 1-7

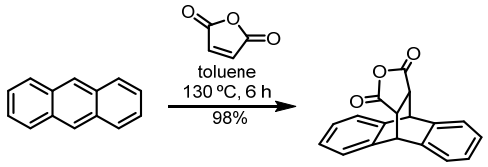

2

Procedure modified from literature.[1] To a round bottom flask were added a stir bar, anthracene (5.34 g, 30 mmol), maleic anhydride (3.04 g, 31 mmol), 90 mL toluene. The reaction mixture was allowed to stir at 130 ºC for 6 hours. The reaction mixture was then cooled to room temperature and the solids were separated by filtration. The solids were then washed with 100 mL hexanes and dried *in vacuo*. The light grey solids were used without further purification. Yield 8.1 g (98%).

^{1}H NMR (600 MHz, $CDCl_3$) δ 7.39 (ddd, 2H), 7.34 (ddt, 2H), 7.24 – 7.17 (m, 4H), 4.83 (t, 2H), 3.53 (dd, 2H).
^{13}C NMR (126 MHz, $CDCl_3$) δ 170.57, 140.79, 138.24, 127.91, 127.30, 125.35, 124.54, 48.15, 45.58.

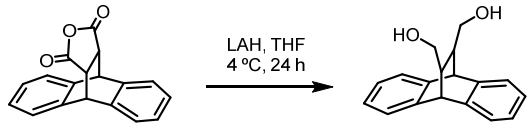

2 **3**

Procedure modified from literature.[2] To a flame-dried 3-neck round bottom flask under positive N_2 pressure were added a stir bar and lithium aluminum hydride (1.7 g, 43.9 mmol). The round bottom was then cooled with an ice bath and was charged with anhydrous THF (234 mL). The slurry was allowed to stir vigorously and compound **2** (8.1 g, 29.3 mmol) was added under positive N_2 via scoop-wise addition over 15 minutes. The reaction mixture was stirred in the ice bath for 4 hours, after which the ice bath was removed. The reaction mixture was allowed to stir at ambient temperature for another 20 hours. The reaction mixture was then cooled again with an ice bath and quenched with slow, sequential addition of 1.7 mL water, 5.3 mL 15%w NaOH, 5 mL water. The quenched mixture was stirred for 1 hour and then filtered. The solids were washed with copious THF. The filtrate was combined and concentrated down *in vacuo* until constant weight was achieved. The white solids were used without further purification.

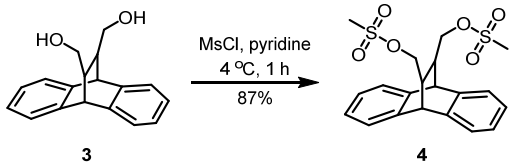

3 4

Procedure modified from literature.[3] To a flame-dried round bottom flask under positive N_2 pressure were added a stir bar and compound **3** (7.5 g, 28.2 mmol). The round bottom was then charged with pyridine (56.4 mL) and slurry was stirred at ambient temperature until all the solids had dissolved. The reaction mixture was then cooled with an ice bath and methyl sulfonyl chloride (5.0 mL, 64.8 mmol) was added dropwise over 15 minutes. The reaction mixture was removed from the ice bath and allowed to stir at ambient temperature for 1 hour. The reaction mixture was then cooled again with an ice bath and quenched with addition of 0.5 mL water. The reaction mixture was then concentrated *in vacuo*. The solids were redissolved in 250 mL DCM and washed 5 times with 1 M HCl. The organic layer was dried with brine and Na_2SO_4, and then the solvent was removed *in vacuo*. The product was used without further purification. Yield 10.3 g (87%).

^{1}H NMR (400 MHz, $CDCl_3$) δ 7.32 (td, 4H), 7.17 (ddd, 4H), 4.40 (d, 2H), 3.99 (dd, 1H), 3.80 – 3.69 (m, 1H), 3.02 (s, 6H), 2.64 – 2.53 (m, 2H).
^{13}C NMR (126 MHz, $CDCl_3$) δ 142.33, 139.85, 126.85, 126.61, 125.78, 123.97, 69.01, 46.04, 40.32, 37.66.

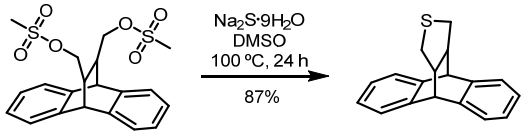

4 5

Procedure modified from literature.[3] To a round bottom flask were added a stir bar, compound **4** (10.3 g, 24.4 mmol), $Na_2S{\cdot}9\ H_2O$ (6.44 g, 26.8 mmol), DMSO (97.6 mL). The round bottom flask was sealed and moved to a 100 ºC oil bath. The reaction mixture was stirred at 100 ºC for 24 hours. The reaction mixture was then allowed to cool to ambient temperature and slowly precipitated into 900 mL of mixture of 4:1 water:acetone. The solids were collected by filtration and used without further purification. Yield 5.6 g (87%).

^{1}H NMR (400 MHz, $CDCl_3$) δ 7.24 (d, 4H), 7.16 – 7.04 (m, 4H), 4.09 (s, 2H), 2.90 (s, 2H), 2.80 (dd, 2H), 2.23 – 2.14 (m, 2H).
^{13}C NMR (126 MHz, cdcl$_3$) δ 144.16, 141.43, 126.17, 125.96, 123.81, 50.92, 48.57, 35.69.

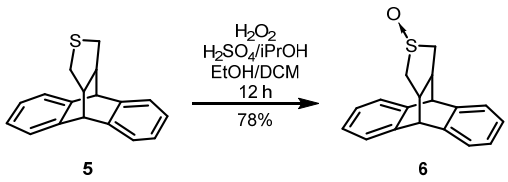

5 6

Procedure modified from literature.[3] To a round bottom flask were added a stir bar, compound **5** (5.6 g, 21.2 mmol), DCM (105 mL), EtOH (105 mL), 0.35 M H_2SO_4 in iPrOH (12.2 mL, 4.4 mmol), 30% hydrogen peroxide (2.24 mL, 22.4 mmol). The reaction was stirred at ambient temperature until all the starting material had been consumed by TLC. The reaction mixture was then diluted with an 150 mL of DCM and quenched with 100 mL of Na_2SO_3 solution. The organic layer was separated and the aqueous layer was extracted 5 times with DCM. The organic layers were combined and concentrated down. The product was purified by column chromatography with 5% MeOH in EtOAc as the running eluent. Yield 4.6 g (78%).

^{1}H NMR (600 MHz, cdcl3) δ 7.40 – 7.26 (m, 2H), 7.21 – 7.07 (m, 2H), 4.22 (d, 1H), 3.57 – 3.31 (m, 1H), 3.08 (ddd, 1H), 1.82 (ddd, 1H).
^{13}C NMR (126 MHz, cdcl$_3$) δ 142.96, 126.39, 126.15, 126.06, 123.76, 77.16, 76.91, 76.65, 54.92, 47.35, 45.20.

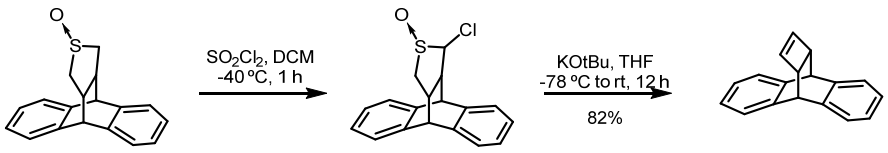

6 7 1

Procedure modified from literature.[3] To a flame-dried round bottom flask were added a stir bar, compound **6** (4.6 g, 16.4 mmol), anhydrous DCM (164 mL), anhydrous pyridine (2.64 mL, 32.8 mmol). SO_2Cl_2 (1.4 mL, 17.22 mmol) was added dropwise over 30 minutes by syringe pump. The reaction mixture was allowed to stir in a -40 ºC cold bath for 1 hour. The reaction was quenched by addition of 150 mL of 1 M HCl and removed from the cold bath. The organic layer was separated, and the aqueous layer was extracted 3 times with 30 mL DCM. The organic layers were dried with Na_2SO_4 and the solvent was removed *in vacuo*. The crude product was used without further purification.

To a flame-dried round bottom flask under positive N_2 pressure were added a stir bar, compound **7** and anhydrous THF (25 mL). The reaction mixture was cooled with a -78 ºC cold bath and KOtBu (5.2 g, 45.92 mmol) in 40 mL THF was added dropwise. The reaction mixture was allowed to stir in the -78 ºC cold bath for 1 hour. After the hour, the reaction mixture was removed from the cold bath and allowed to stir at ambient temperature for 12 hours. The reaction mixture was then concentrated down to 10% the

original volume and rediluted with DCM. The reaction mixture was then cooled with an ice bath and quenched by slow addition of 50 mL 1 M HCl. The organic layer was separated and the aqueous layer was exctracted 3 times with 50 mL DCM. The organic layers were combined and the yellow solids were purified by column chromatography using 10%v toluene in hexanes as the running solvent. The white solids were then triturated in a small volume of cold hexanes. Yield 3.1 g of **1** (82%).

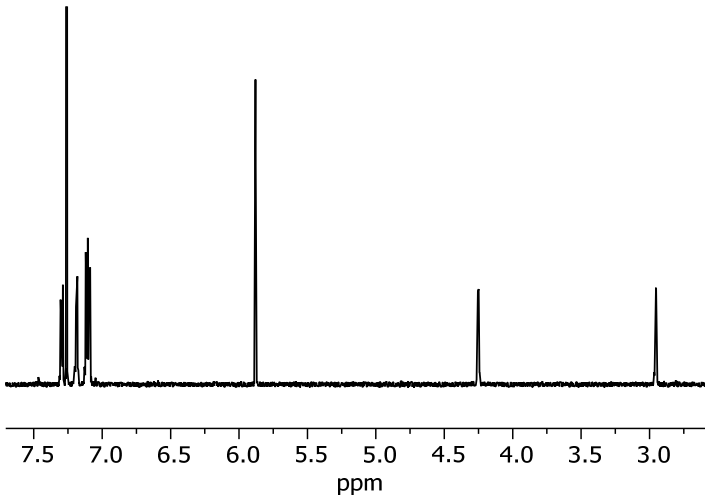

^{1}H NMR (500 MHz, $CDCl_3$) δ 7.32 – 7.24 (m, 2H), 7.19 (dd, J = 5.4, 3.2 Hz, 2H), 7.15 – 7.07 (m, 4H), 5.88 (d, J = 0.7 Hz, 2H), 4.28 – 4.23 (m, 2H), 2.96 (ddd, J = 2.8, 1.3, 0.7 Hz, 2H).

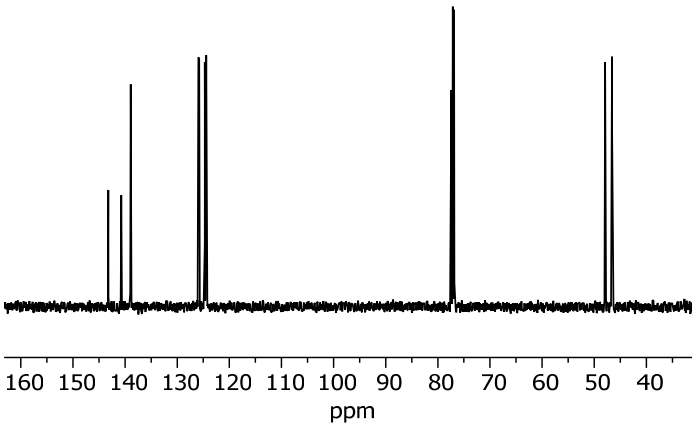

^{13}C NMR (126 MHz, $CDCl_3$) δ 143.26, 140.76, 138.96, 125.97, 125.82, 124.73, 124.46, 47.93, 46.62.

MS: m/z calculated for $C_{18}H_{14}$ $[M]^+$:231.11; found: 231.17.

S2.2. Synthetic procedure for reference diene-compounds (11/17/18)

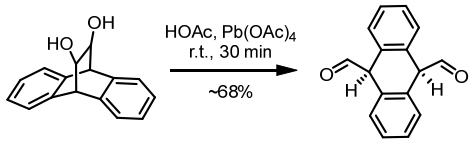

8 9

Cis-9,10-dihydroanthracene-9,10-dicarboaldehyde **9**: Compoumd **9** was synthesized according to reported procedure.[4] To a flame-dried 50 mL round-bottomed flask equipped with a magnetic stir bar was added **8** (709 mg, 3.0 mmol), followed by glacial acetic acid (13 mL). The mixture was stirred until complete dissolution was observed. Lead(IV) acetate (1.46 g, 3.3 mmol, 1.1 equiv.) was added portionwise over 10 minutes. After complete addition, the resulting yellow solution was stirred at ambient temperature for 30 minutes, during which time the reaction progress was monitored by TLC. Upon completion, the reaction mixture was cooled to 15 °C in an ice-water bath and filtered through a medium-porosity sintered glass funnel. The collected solid was washed sequentially with cold water (3 × 10 mL) until the washings were neutral to pH paper. The product was dried under reduced pressure (0.1 mmHg) at 40 °C for 12 hours to afford **9** as a light yellow crystalline solid (482 mg, 68% yield).

^{1}H NMR (600 MHz, $CDCl_3$) δ 9.45 (d, 1H), 7.43 (s, 4H), 4.96 (d, 1H).

^{13}C NMR (101 MHz, $CDCl_3$) δ 196.39, 130.33, 129.62, 128.68, 60.03.

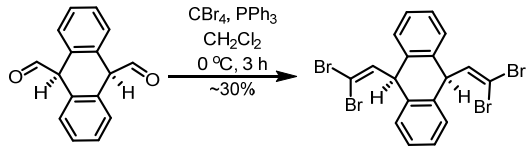

9 10

cis-9,10-Bis(2,2-dibromovinyl)-9,10-dihydroanthracene **10**: To a flame-dried 25 mL round-bottomed flask equipped with a magnetic stir bar and a rubber septum was added **9** (276 mg, 1.17 mmol) and triphenylphosphine (2.03 g, 7.7 mmol, 6.6 equiv.). The solids were placed under an inert atmosphere followed by addition of dichloromethane (5 mL) via syringe. The resulting solution was cooled to 0 °C in an ice-water bath. Carbon tetrabromide (1.70 g, 5.14 mmol, 4.4 equiv.) was dissolved in dichloromethane (2.5 mL) in a separate vial. This solution was transferred to the reaction flask dropwise via syringe over 5 minutes while maintaining the internal temperature below 5 °C. After complete addition, the cooling bath was removed, and the reaction mixture was allowed to warm to ambient temperature with continued stirring. The reaction progress was monitored by TLC (hexanes/ethyl acetate, 9:1), and the mixture was

stirred for 3 hours until complete consumption of the starting material was observed. Upon completion, the reaction mixture was concentrated under reduced pressure. The crude residue was purified by recrystallization from methanol (approximately 15 mL). The crystalline product was collected by vacuum filtration, washed with cold methanol (2 × 5 mL), and dried under high vacuum (0.1 mmHg) at 40 °C for 12 hours to afford **10** as a pale yellow crystalline solid (224 mg, 35% yield).

^{1}H NMR (600 MHz, $CDCl_3$) δ 7.39 (dd, *J* = 5.7, 4H), 7.30 (dd, *J* = 5.7, 4H), 6.35 (d, 2H), 5.10 (d, 2H).

^{13}C NMR (101 MHz, $CDCl_3$) δ 140.84, 134.27, 128.53, 127.82, 89.51, 47.66.

MS: m/z calculated for $C_{18}H_{12}Br_4$ $[M]^+$:547.76; found: 547.77.

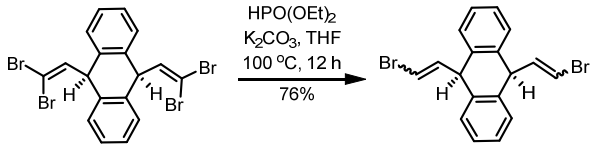

10 **11**

Cis-9,10-Bis(2-bromovinyl)-9,10-dihydroanthracene **11**: A 10 mL pressure tube equipped with a magnetic stir bar was flame-dried under vacuum and cooled under a stream of nitrogen. **10** (385 mg, 0.70 mmol), anhydrous potassium carbonate (388 mg, 2.8 mmol, 4.0 equiv.), and diethyl phosphite (776 mg, 0.72 mL, 5.6 mmol, 8.0 equiv.), anhydrous THF (3 mL) were added under nitrogen and the tube was sealed. The reaction mixture was stirred vigorously at 100 °C for 16 hours, during which time the reaction progress was monitored by TLC. After cooling to ambient temperature, the reaction was quenched by the addition of saturated aqueous sodium carbonate solution (6 mL). The mixture was transferred to a separatory funnel and extracted with ethyl acetate (3 × 10 mL). The combined organic layers were washed with brine (15 mL), dried over anhydrous magnesium sulfate, filtered, and concentrated under reduced pressure. The crude product was purified by column chromatography on silica gel (60-120 mesh) using n-hexane as the eluent. The product-containing fractions were combined and concentrated under reduced pressure to afford **11** as a white solid (206 mg, 75.5% yield) consisting of a mixture of EE/ZE/ZZ stereoisomers.

^{1}H NMR (600 MHz, $CDCl_3$) (EE isomer): δ 7.29 (m, 8H), 6.27 (d, 2H), 5.95 (d, 2H), 4.64 (dd, 2H).

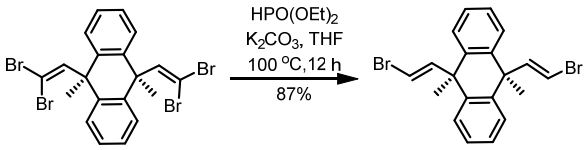

12 13

9,10-bis(E-2-bromovinyl)-9,10-dimethyl-9,10-dihydroanthracene **13**: A 10 mL pressure tube equipped with a magnetic stir bar was flame-dried under vacuum, **12** (230 mg, 0.40 mmol), anhydrous potassium carbonate (221 mg, 1.6 mmol, 4.0 equiv.), diethyl phosphite (442 mg, 0.41 mL, 3.2 mmol, 8.0 equiv.) and anhydrous THF (1 mL) were added sequentially under nitrogen and the tube was sealed. The heterogeneous reaction mixture was stirred vigorously at 100 °C for 16 hours, during which time the reaction progress was monitored by TLC. After cooling to ambient temperature, the reaction was quenched by the addition of saturated aqueous sodium carbonate solution (2 mL). The mixture was transferred to a separatory funnel and extracted with ethyl acetate (3 × 5 mL). The combined organic layers were washed sequentially with water (5 mL) and brine (5 mL), dried over anhydrous magnesium sulfate, and concentrated under reduced pressure. The crude product was purified by column chromatography on silica gel (60-120 mesh) using n-hexane as the eluent. The product-containing fractions were combined and concentrated under reduced pressure to afford **13** as a white crystalline solid (145.5 mg, 87% yield) with exclusively E-stereochemistry at both vinyl bromide moieties.

^{1}H NMR (500 MHz, $CDCl_3$) δ 7.39 (dd, 4H), 7.31 (dd, 4H), 6.56 (d, 2H), 6.40 (d, 2H), 1.64 (s, 6H).

^{13}C NMR (101 MHz, $CDCl_3$) δ 145.38, 138.22, 128.28, 127.18, 104.71, 46.47, 32.34.

MS: m/z calculated for $C_{20}H_{18}Br_2$ $[M+Na]^+$:440.97; found: 440.31.

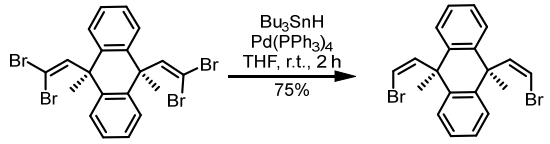

12 14

9,10-bis(Z-2-bromovinyl)-9,10-dimethyl-9,10-dihydroanthracene **14**: A 10 mL pressure tube equipped with a magnetic stir bar was flame-dried under vacuum. Tetrakis(triphenylphosphine)palladium(0) (89 mg, 0.08 mmol, 12 mol%), **12** (372 mg, 0.65 mmol) and anhydrous THF (7.5 mL) was added under nitrogen, then tributyltin hydride (415 mg, 0.38 mL, 1.42 mmol, 2.2 equiv.) was added dropwise over 5 minutes. The tube was sealed solution was stirred at ambient temperature for 2 hours. Upon completion, the reaction was quenched by the addition of saturated aqueous

ammonium chloride solution (2 mL). The mixture was transferred to a separatory funnel, diluted with ethyl acetate (15 mL). The organic layer was washed sequentially with aqueous potassium fluoride solution (1.0 M, 3 × 10 mL) to remove organotin byproducts, followed by brine (10 mL). The organic phase was dried over anhydrous magnesium sulfate and concentrated under reduced pressure. The crude product was purified by column chromatography on silica gel (60-120 mesh) using a mixture of n-hexane/ethyl acetate/triethylamine (100:5:2.5 v/v/v) as the eluent. The product-containing fractions were combined and concentrated under reduced pressure. The resulting solid was recrystallized from hot n-hexane to remove residual tributyltin byproducts. The purified crystals were collected by filtration, washed with cold methanol, and dried under high vacuum (0.1 mmHg) at 40 °C for 12 hours to afford **14** as a white crystalline solid (203 mg, 75% yield) with Z-stereochemistry at both vinyl bromide moieties.

^{1}H NMR (600 MHz, $CDCl_3$) δ 7.36 (dd, 4H), 7.22 (dd, 4H), 6.76 (d, 2H), 6.30 (d, 2H), 1.84 (s, 6H).

^{13}C NMR (151 MHz, $CDCl_3$) δ 142.89, 139.89, 127.80, 126.74, 106.62, 45.67, 36.65.

MS: m/z calculated for $C_{20}H_{18}Br_2$ $[M+Na]^+$:440.97; found: 440.89.

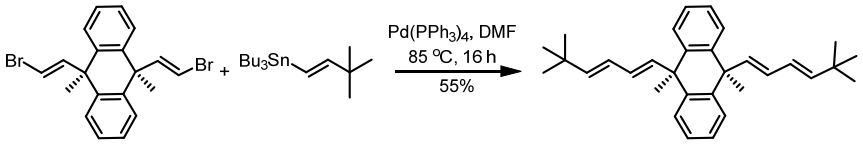

13 15

9,10-bis(5,5-dimethyl-1E,3E-hexadienyl)-9,10-dimethyl-9,10-dihydroanthracene **15**: A 5 mL pressure tube equipped with a magnetic stir bar was flame-dried under vacuum. Tetrakis(triphenylphosphine) palladium(0) (23.1 mg, 0.02 mmol, 20 mol%), **13** (41.8 mg, 0.10 mmol), (E)-tributyl(3,3-dimethylbut-1-enyl)tin (82.1 mg, 0.22 mmol, 2.2 equiv.) and anhydrous DMF (1 mL) were added under nitrogen. The tube was sealed and the resulting solution was stirred at 80 °C for 16 hours. The reaction progress was monitored by TLC (hexanes/ethyl acetate, 10:1). After cooling to ambient temperature, the reaction mixture was diluted with ethyl acetate (10 mL) and washed sequentially with aqueous potassium fluoride solution (1.0 M, 3 × 5 mL) to remove organotin byproducts, water (5 mL), and brine (5 mL). The organic phase was dried over anhydrous magnesium sulfate and concentrated under reduced pressure at 40 °C. The crude product was purified by column chromatography on silica gel (60-120 mesh) using a mixture of n-hexane/ethyl acetate (10:1 v/v) as the eluent to afford **15** as a white crystalline solid (23.4 mg, 54.8% yield) with all-E stereochemistry in the conjugated diene systems.

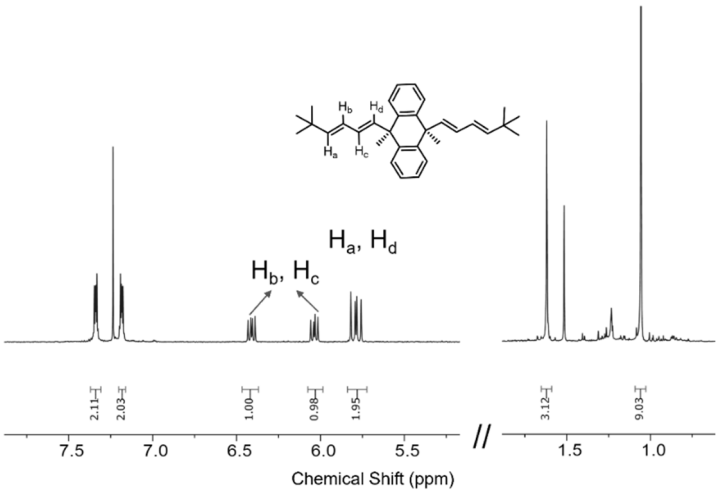

^{1}H NMR (500 MHz, $CDCl_3$) δ 7.38 (dd, 4H), 7.23 (dd, 4H), 6.45 (dd, 2H), 6.08 (dd, 2H), 5.83 (t, 4H), 1.67 (s, 6H), 1.10 (s, 18H).

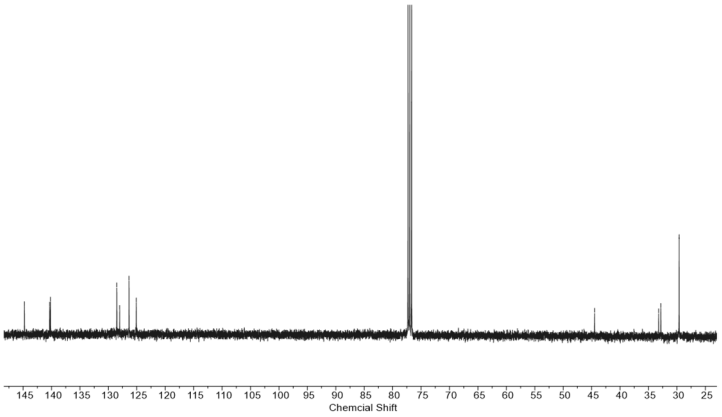

^{13}C NMR (101 MHz, $CDCl_3$) δ 144.77, 140.33, 140.18, 128.51, 128.02, 126.37, 125.08, 44.48, 33.22, 32.83, 29.61.

MS: m/z calculated for $C_{32}H_{40}$ $[M+H]^+$:425.32; found: 425.47.

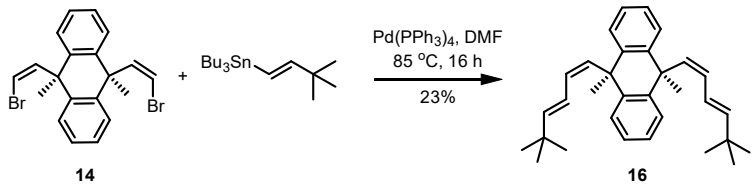

14 16

9,10-bis(5,5-dimethyl-1Z,3E-hexadienyl)-9,10-dimethyl-9,10-dihydroanthracene **16**: A 5 mL pressure tube equipped with a magnetic stir bar was flame-dried under vacuum. Tetrakis(triphenylphosphine)palladium(0) (23.1 mg, 0.02 mmol, 20 mol%), **14** (41.8 mg, 0.10 mmol), (E)-tributyl(3,3-dimethylbut-1-enyl)tin (82.1 mg, 0.22 mmol, 2.2 equiv.) and anhydrous DMF (1 mL) were added under nitrogen. The tube was sealed and the resulting yellow solution was stirred at 85 °C for 16 hours. The reaction progress was monitored by TLC (hexanes/ethyl acetate, 20:1). After cooling to

ambient temperature, the reaction mixture was diluted with ethyl acetate (10 mL) and washed sequentially with aqueous potassium fluoride solution (1.0 M, 3 × 5 mL) to remove organotin byproducts, water (5 mL), and brine (5 mL). The organic phase was dried over anhydrous magnesium sulfate and concentrated under reduced pressure. The crude product was purified by column chromatography on silica gel (60-120 mesh) using a mixture of n-hexane/ethyl acetate (20:1 v/v) as the eluent to afford **16** as a white solid (10 mg, 23% yield) with Z,E-stereochemistry for the conjugated diene.

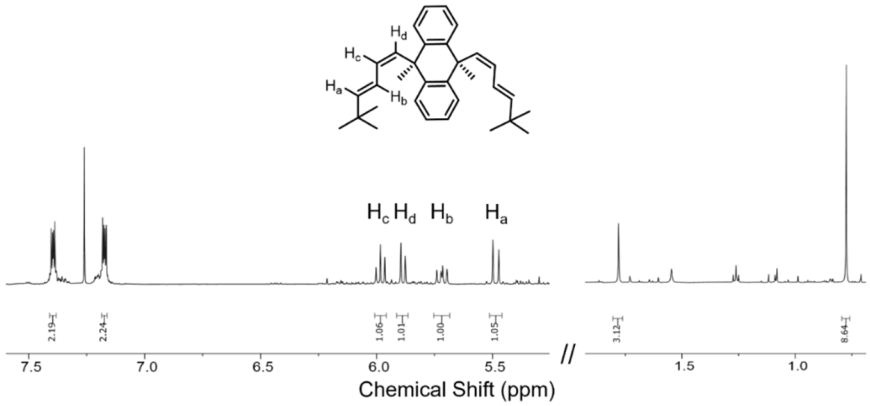

^{1}H NMR (600 MHz, $CDCl_3$) δ 7.37 (dd, 4H), 7.15 (dd, 4H), 5.96 (t, 2H), 5.86 (d, 2H), 5.69 (s, 2H), 5.46 (d, 2H), 1.76 (s, 6H), 0.75 (s, 18H).

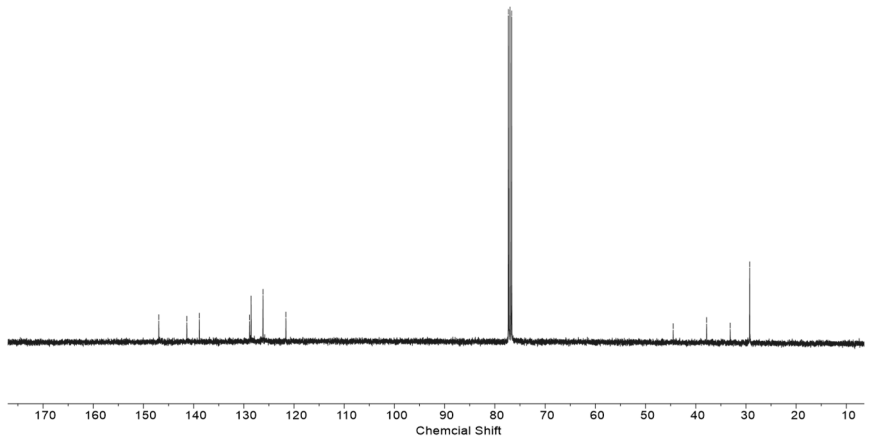

^{13}C NMR (101 MHz, $CDCl_3$) δ 146.93, 141.34, 138.85, 128.84, 128.55, 126.18, 121.62, 44.48, 37.84, 33.13, 29.25.

MS: m/z calculated for $C_{32}H_{40}$ $[M+H]^+$:425.32; found: 425.36

S2.3. Synthetic procedure for poly1

To a vial in a N_2 glove box were added **1** (135.6 mg, 0.5889 mmol), toluene (1.37 mL), and 0.1 mL of a stock solution of Grubbs 2nd generation catalyst (0.5 mg/0.1 mL toluene, 0.0005889 mmol). The reaction mixture was capped and removed from the glove box and heated to 60 ºC to 24 hours. The reaction mixture was then quenched by addition of 1 drop of ethyl vinyl ether and allowed to stir for 5 minutes. The polymer was precipitated into methanol and the residual solvent was removed *in vacuo*.

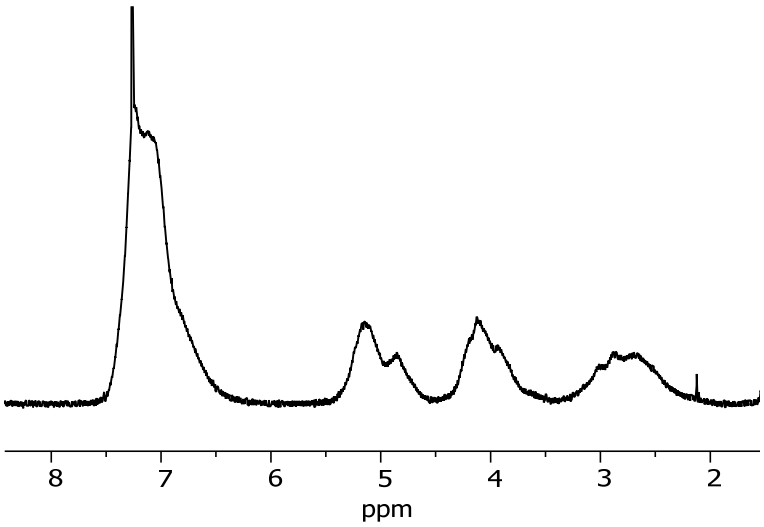

^{1}H NMR (600 MHz, $CDCl_3$) δ 7.64-6.26 (br, 8H), 5.58-4.48 (br, 2H), 4.48-3.41 (br, 2H), 3.40-2.10 (br, 2H).

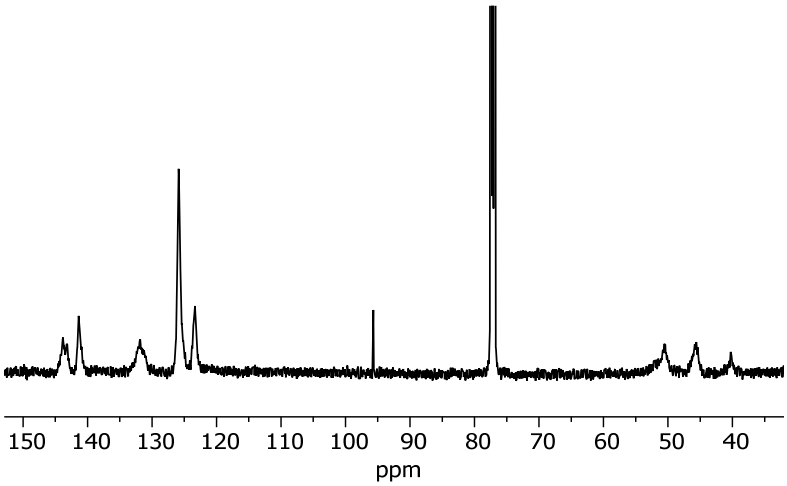

^{13}C NMR (126 MHz, $CDCl_3$) δ 143.80, 143.24, 141.33, 131.82, 125.86, 123.39, 50.60, 45.66, 40.22.

S3. Design of reference compounds representing mechanochemically ring-opened repeat unit structures.

To synthesize a reference compound for the expected *syn*-dibutadienyl-dihydroanthracene structure of the mechanochemically ring-opened repeat unit, we first prepared **11** through reductive debromination of 9,10-bis(2,2-dibromovinyl)-9,10-dihydroanthracene **10** in EE/EZ/ZZ stereoisomers. Various attempts at cross-coupling reactions of compound **11** with either tributyl(tert-butylvinyl)tin (Stille reaction) or 2-propylvinylboronic acid (Suzuki reaction) to produce the desired dibutadienyl substituents resulted in complex product mixtures that were inseparable (**Scheme S1**). We attributed the poor reactivity to the acidic benzylic protons at the 9,10-positions of the dihydroanthracene core, which can undergo competitive deprotonation under the basic reaction conditions typically employed in cross-coupling reactions.

Alternatively, we synthesized methyl substituted 9,10-bis(bromovinyl)-9,10-dihydroanthracene **12** with exclusive E (**13**) or Z (**14**) configuration via two different reductive debromination methods. **13** or **14** was found to undergo Stille reaction smoothly with tributyl(tert-butylvinyl)tin, leading to the methyl substituted reference compound **15** or **16** with EE or ZE diene configuration (**Scheme S2**). The alkene proton signals of **15** and **16** can be clearly assigned based on the coupling constants and chemical shifts, and were used to guide the peak assignment of mechanochemically transformed polymer.

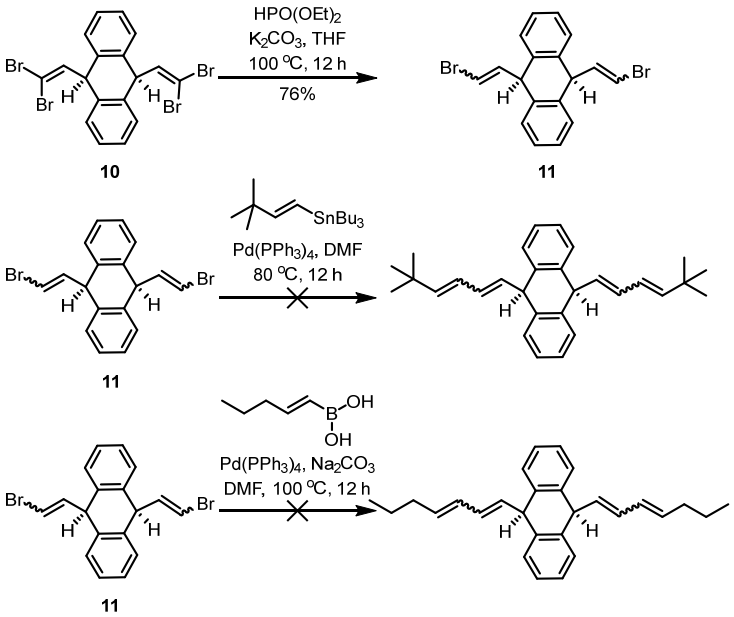

Scheme S1. Attempted synthesis of 9,10-dienyl-9,10-dihydroanthracene reference compounds (**12**/**13**).

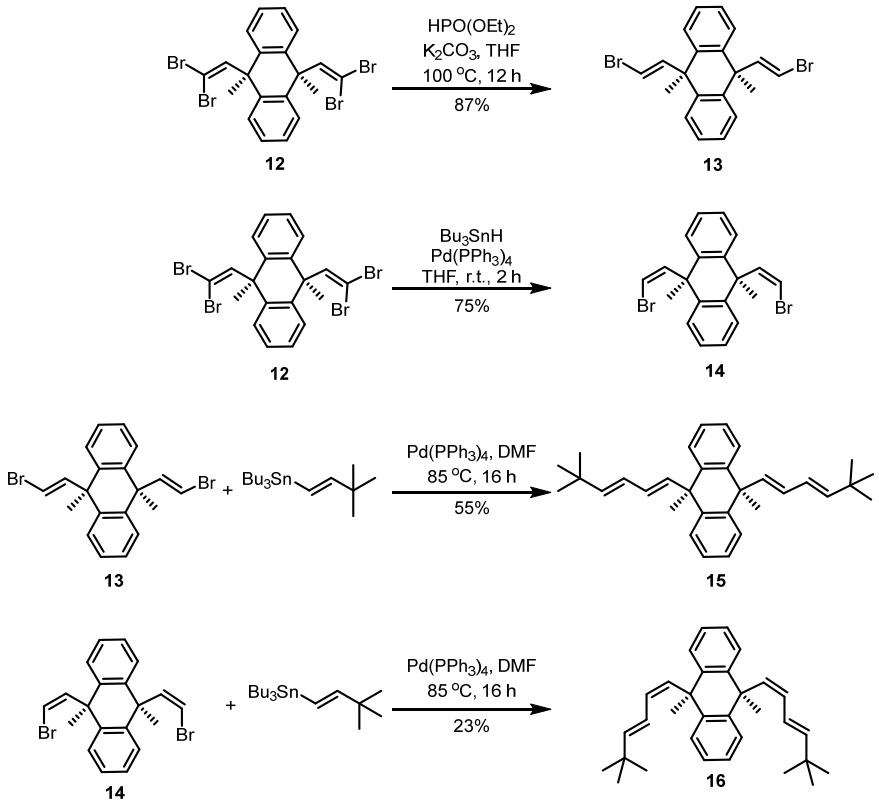

Scheme S2. Synthesis of 9,10-dimethyl-9,10-dienyl-9,10-dihydroanthracene reference compounds (**15**/**16**).

S4. Calculation of mechanoactivation percentage based on NMR analysis.

The NMR signals of **poly1** were assigned as noted in **Figure S1** with the correct integration. New signals emerged after sonication of **poly1** overlapped with the signals at 4.5-5.5 ppm (protons a) and 6.5-7.5 ppm (protons d) of remaining **poly1**. But using the signals at 2.2-3.5 ppm (protons b) and 3.5-4.5 ppm (protons c) of remaining **poly1**, which integrate at 1:1, the integration of newly generated signals at 4.5-5.5 ppm and 6.5-7.5 ppm regions can be calculated by subtracting the signal intensity of remaining **poly1**. Furthermore, the signals in the 5.5-6.5 ppm region (protons b') from sonicated **poly1** do not overlap with any signals from **poly1**, and these signals integrate with the newly generated signals at 4.5-5.5 ppm and 6.5-7.5 ppm at 1:1:1 ratio. Therefore, we used two ways to calculate the degree of activation and *both methods gave nearly identical results*: method A) integration at 5.5-6.5 ppm (signals from activated **poly1**) is compared to integration at 3.5-4.5 ppm (signals from remaining **poly1**); method B) integration at 4.5-6.5 ppm subtracts integration at 3.5-4.5 ppm or 2.2-3.5 ppm and the calculated signal intensity from

activated **poly1** is compared to integration at 3.5-4.5 ppm (signals from remaining **poly1**). An exemplary calculation of mechanoactivation percentage using method B is given below:

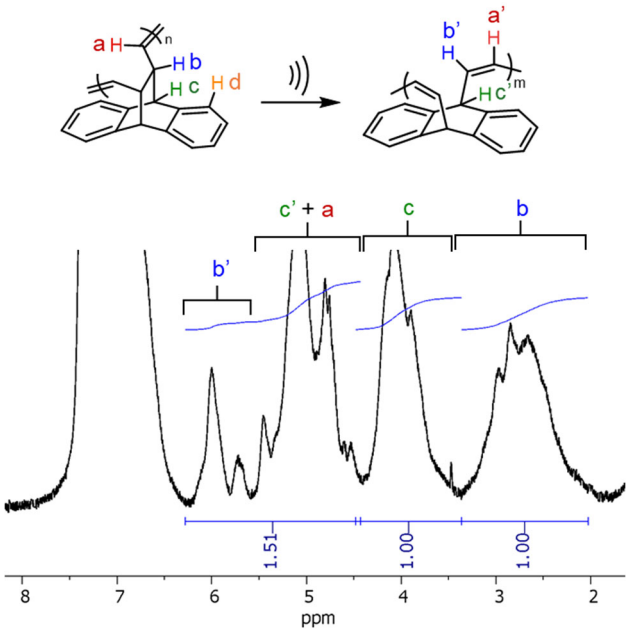

$$\%\ mechanoactivation = \frac{\frac{(1.51-1)}{2}}{\frac{(1.51-1)}{2}+1} = 20.3\%$$

Figure S1. Exemplary ^{1}H NMR spectrum of sonicated **poly1**, showing the integration used to calculate mechanoactivation percentage.

S5. Control polymers

S5.1. Synthetic procedure for poly1-H_2 and its attempted mechanoactivation.

To a round bottom flask were added, **poly1** (53.9 mg, 0.234 mmol with respect to repeat unit), toluene (4.7 mL), p-toluene sulfonyl hydrazide (218 mg, 1.17 mmol), triethylamine (0.212 mL, 1.521 mmol). The reaction mixture was moved to a heated oil bath and refluxed for 22 hours. The reaction mixture was then allowed to cool to room temperature and the polymer was purified by successive precipitation into methanol until all the yellow color had been removed, about 3-5 times. By comparing the integration of the benzylic protons to the residual alkene signals, we determined that this polymer is 77% hydrogenated.

Sonication of hydrogenated **poly1** under standard conditions resulted in no observable change in the NMR spectrum (**Fig. S2**).

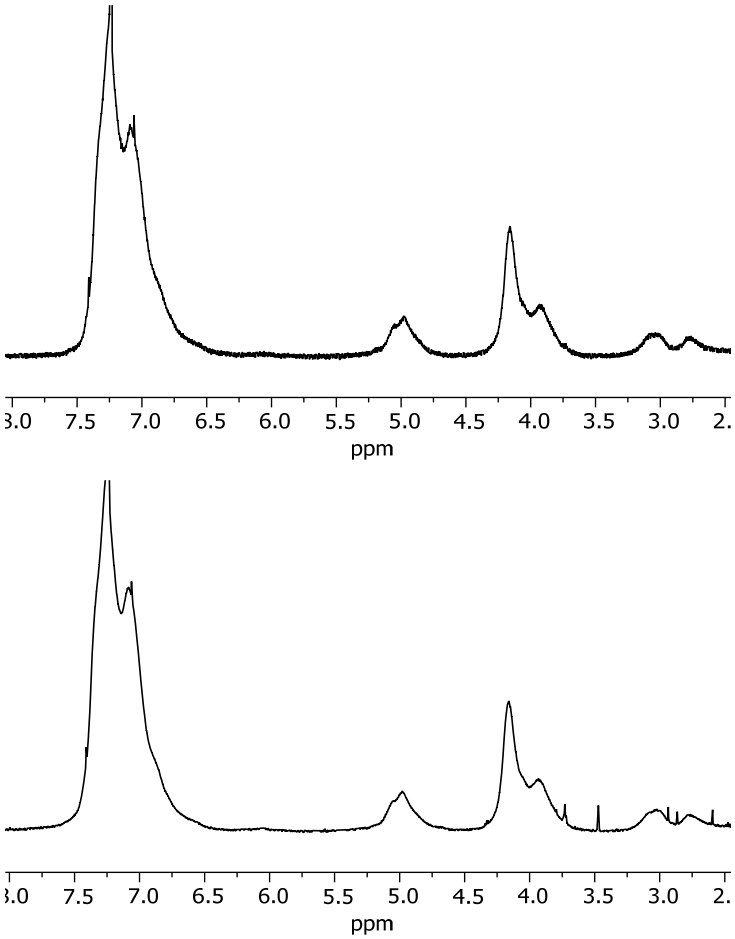

Figure S2. ^{1}H NMR spectra of hydrogenated **poly1** DP 1000 before (top) and after (bottom) sonication. No changes observed after 3.5 h of sonication.

S5.2. Synthetic procedure for poly(1-*co*-DHF) and its attempted mechanoactivation.

To a vial in a N_2 glove box were added **1** (135.6 mg, 0.5889 mmol), dihydrofuran (41.3mg, 44.5 µL, 0.5889 mmol), and 0.1 mL of a stock solution of Grubbs 2nd generation catalyst (1 mg/0.1 mL toluene, 0.0011778 mmol). The reaction mixture was capped and removed from the glove box and heated to 40 ºC to 24 hours. The polymer was dissolved in DMAP in THF (1 mL). The polymer was precipitated into a solution of 1:2 H_2O_2 : 15% NaOH. The precipitate was collected and the residual solvent was removed *in vacuo*.

Sonication of **poly(1-*co*-DHF)** under standard conditions resulted in no observable change in the NMR spectrum. Sonication of **poly(1-*co*-DHF)** in the presence of a large excess of potent hydrogen atom donor (using 1,4-cyclohexadiene as the solvent) or trapping agent for diradical species (0.1 M tetracyanoethylene) still resulted in no observable change in the NMR spectrum (**Figure S4**).

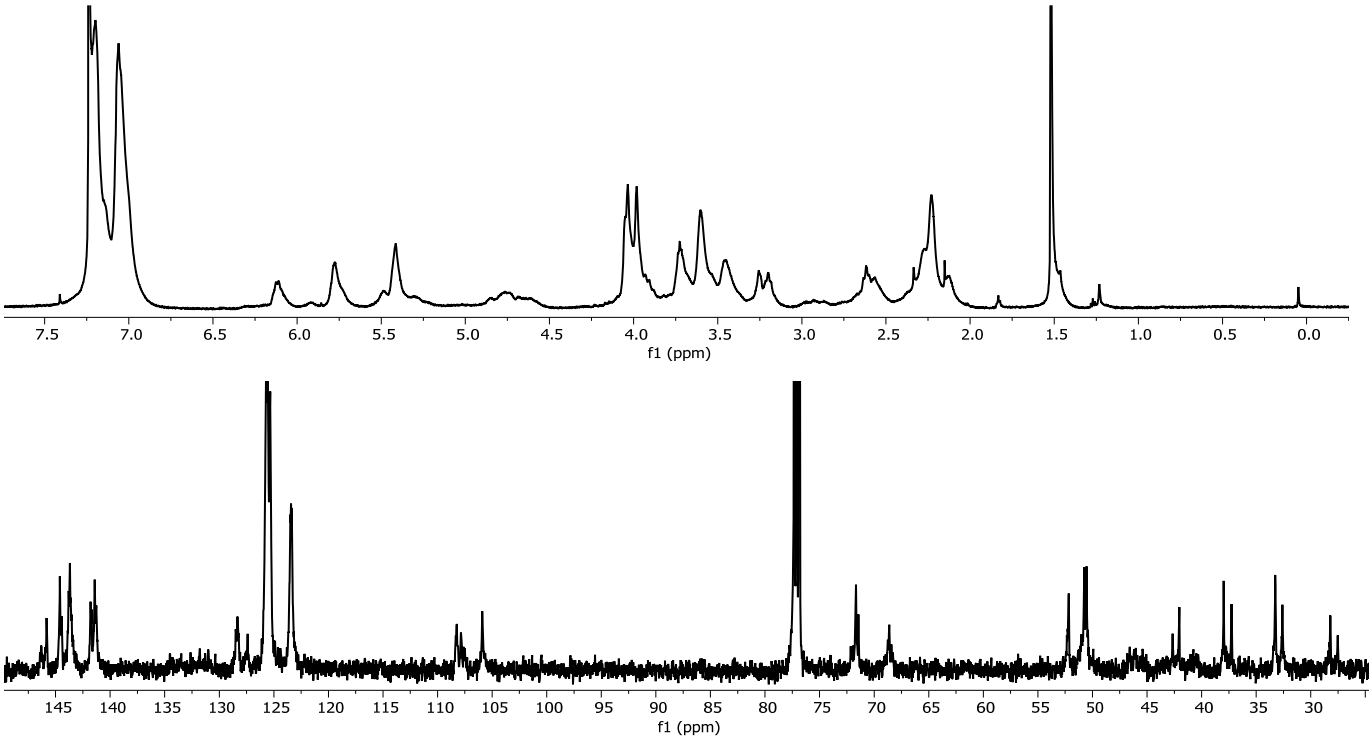

Figure S3. ^{1}H (top) and ^{13}C (bottom) NMR spectrum of **poly(1-*co*-DHF)**, showing no observable signals from benzobarrelane homo-dyads.

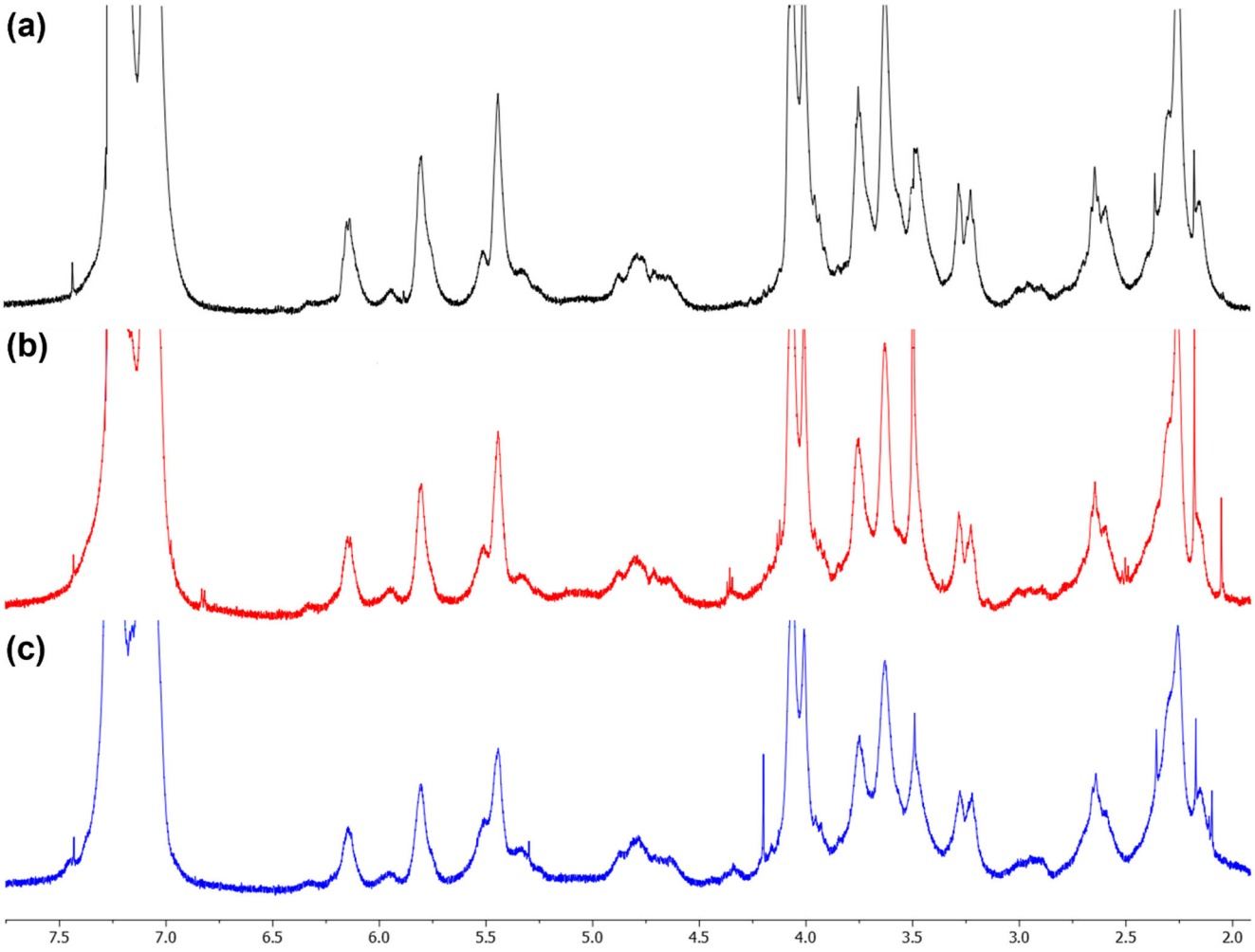

Figure S4. ^{1}H NMR spectra of **poly(1-*co*-DHF)** (a) before sonication, (b) after sonication in 1,4-cyclohexadiene as the solvent, (c) and after sonication in THF with 0.1 M tetracyanoethylene. No changes observed after 1.5 h of sonication.

S6. Computational details

S6.1. Computational methods

The XYZ coordinate files of all the geometry structures are deposited at Zotero for this publication (https://doi.org/ 10.5281/zenodo.15870740).

The mechanochemical activation of benzobarrelanes is computationally studied using the GPU-accelerated electronic structure software TeraChem.[5-8] The external pulling forces, f_{ext}, are applied at the two terminal carbon atoms at each end of the modeling unit. The resulting force potential is modeled as the work induced by this external force, $f_{ext} \cdot x$, where x is the distance between the two terminal carbon-pulling atoms. Adding this force potential to the electronic energy of the molecular unit yields the Force-Modified Potential Energy Surface (FMPES).[9]

$$E_{FMPE} = E_{elec} - f_{ext} \cdot x$$

In the above equation, the electronic energy, E_{elec}, was computed using the unrestricted B3LYP density functional on a 6-31G* basis set with Grimme's third generation empirical dispersion[10] (UB3LYP-D3/6-31G* level of theory). The external force, f_{ext}, can be directly specified in each simulation, and we will simply note this force as f in later texts and figures.

Computations of benzobarrelane mechanochemistry involve *ab initio* steered molecular dynamics (AISMD),[9] geometry optimization, transition state search, hessian calculations, and microkinetic modeling. AISMD simulations were performed in the microcanonical ensemble (NVE) for 5 ps for pulling on a benzobarrelane tetramer. All AISMD runs were simulated with initial temperature 300 K and 1.0 fs time step. For the geometry optimization of reactants, products, and transition states, the DL-FIND optimization library[11] was used in TeraChem. During the transition state optimization, the communication between TeraChem and DL-FIND was done with ChemShell.[12] For transition state configurations, first-order saddle points were obtained using the Dimer method,[13-14] and confirmed by one imaginary frequency through the Hessian calculations. To compute the Gibbs free energy of the considered species, the rigid-rotor approximation was used in combination with a modified harmonic approximation, where small vibrational frequencies below 100 cm^{-1} were scaled to this value in order to avoid divergence of the entropic contribution of low-frequency modes. Force-modified minimum energy paths (MEPs) of the ring opening reactions (i.e., **Fig. 6b** in the main text) were calculated using the intrinsic reaction coordinates (IRC)[15] calculations in ChemShell linked to TeraChem. The microkinetic modeling was performed by solving the system ordinary differential equations (ODEs) of the species mole fractions. Numerical integration was performed using the backward differentiation formula (BDF). The kinetic rate coefficients

of each reaction were estimated using the transition state theory[16-18] and the Gibbs free energies of the species. Details of all the calculations are also described in later sections.

S6.2. *Ab initio* steered molecular dynamics

We first used AISMD to simulate the dynamics of the benzobarrelane mechanoactivation. We chose a tetramer system (**Fig. S5**) that contains four repeating units in **poly1**, the outermost carbon atoms (highlighted as red in **Fig. S5**) were chosen as the pulling points such that the external force is applied to the tetramer system. 30 AISMD simulations (listed in **Table S3**) were performed in the microcanonical ensemble (NVE) for 5 ps for tetramer benzobarrelane with external force f = 2.5 nN. All AISMD runs were simulated with initial temperature at 300 K and a 1.0 fs time step. The initial geometry starts from the optimized geometry of a tetramer without force pulling (**Fig. S5a**). Among the 30 AISMD simulations, 23 runs ended up with fully activated tetramer (**Fig. S5b**) within the 5 ps simulation time.

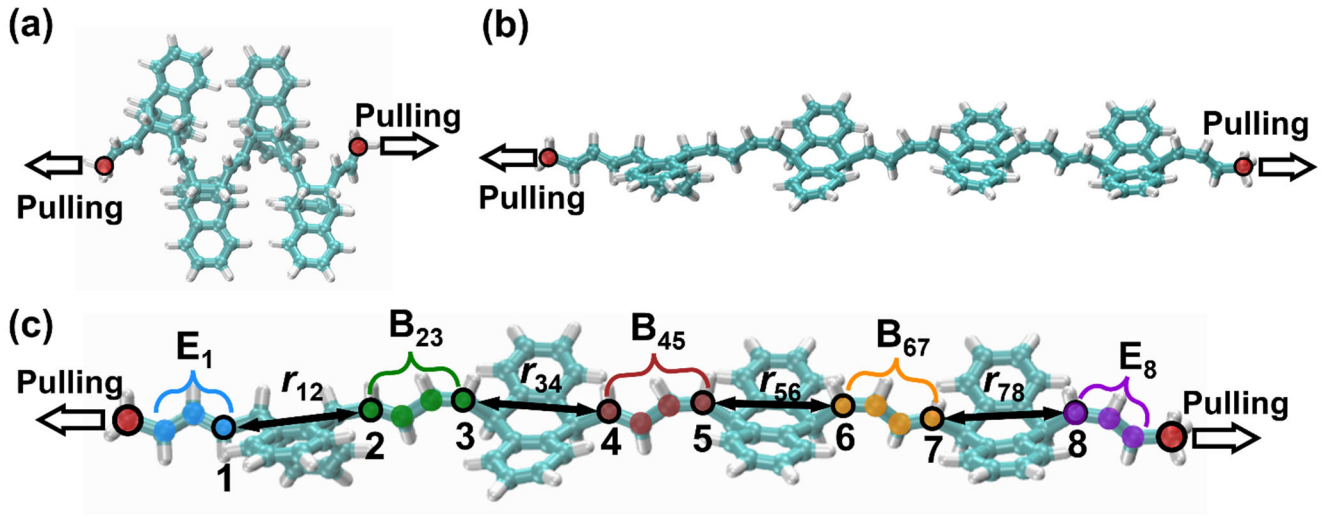

Figure S5. Tetramer system for the *ab initio* molecular dynamics (AISMD) simulations. The pulling points, as the two terminal carbon atoms, are highlighted in red in each panel. **(a)** The initial tetramer geometry at t = 0, representing the minimum-energy, geometry optimized tetramer reactant. **(b)** A representative fully activated tetramer structure after an AISMD simulation. **(c)** Labels used for later AISMD plots, including indices of carbon atoms in the four breaking bonds and their bond lengths (r_{ij}), dienes at the tetramer edge (E_k), and bridge diene between two benzobarrelane units (B_{mn}).

Table S3 and **Fig. S6** provides a summary of the 30 AISMD runs. **Fig. S7-S9** shows the evolutions of the four opening bond lengths and atomic spin densities for all the 30 AISMD simulations. Specifically, **Fig. S7** includes Run 1-21, where all units were activated into biradical products, **Fig. S8** shows Run 24-

29, where only three or two units were activated into biradical products, and **Fig. S9** shows Run 22, 23, and 30, where the mechanoactivation led to tetra-radical products.

Table S3. List of 30 AISMD runs on mechanoactivation of a benzobarrelane tetramer.

Run	Num. of act. units	Bond activation sequence[a]	Radical character (spin multiplicity)
1	4	34 ⇒ 56 ⇒ 78 ⇒ 12	biradical (triplet)
2	4	12 ⇒ 34 ⇒ 56 ⇒ 78	biradical (triplet)
3	4	34 ⇒ 12 ⇒ 56 ⇒ 78	biradical (triplet)
4	4	34 ⇒ 12 ; 78 ⇒ 56	biradical (triplet)
5	4	34 ⇒ 56 ⇒ 78 ⇒ 12	biradical (triplet)
6	4	34 ⇒ 56 ⇒ 12 ⇒ 78	biradical (triplet)
7	4	34 ⇒ 56 ⇒ 78 ⇒ 12	biradical (triplet)
8	4	34 ⇒ 56 ⇒ 78 ⇒ 12	biradical (triplet)
9	4	34 ⇒ 12 ⇒ 56 ⇒ 78	biradical (triplet)
10	4	34 ⇒ 12 ⇒ 56 ⇒ 78	biradical (triplet)
11	4	56 ⇒ 78 ⇒ 34 ⇒ 12	biradical (triplet)
12	4	56 ⇒ 78 ⇒ 34 ⇒ 12	biradical (triplet)
13	4	56 ⇒ 34 ⇒ 78 ⇒ 12	biradical (triplet)
14	4	34 ⇒ 12 ⇒ 56 ⇒ 78	biradical (triplet)
15	4	34 ⇒ 12 ⇒ 56 ⇒ 78	biradical (triplet)
16	4	56 ⇒ 78 ⇒ 34 ⇒ 12	biradical (triplet)
17	4	34 ⇒ 12 ⇒ 56 ⇒ 78	biradical (triplet)
18	4	56 ⇒ 78 ⇒ 34 ⇒ 12	biradical (triplet)
19	4	34 ⇒ 56 ⇒ 12 ⇒ 78	biradical (triplet)
20	4	34 ⇒ 56 ⇒ 12 ⇒ 78	biradical (triplet)
21	4	34 ⇒ 12 ⇒ 56 ⇒ 78	biradical (triplet)
22	4	12 ; 56 ⇒ 34 ; 78	tetra-radical (quintet)
23	4	34 ⇒ 12 ; 78 ⇒ 56	tetra-radical (quintet)
24	3	34 ⇒ 56 ⇒ 78	biradical (triplet)
25	3	34 ⇒ 12 ⇒ 56	biradical (triplet)
26	3	34 ⇒ 56 ⇒ 78	biradical (triplet)
27	3	34 ⇒ 12 ⇒ 56	biradical (triplet)
28	3	56 ⇒ 34 ⇒ 12	biradical (triplet)
29	2	34 ⇒ 56	biradical (triplet)
30	3	34 ; 78 ⇒ 12	tetra-radical (quintet)

[a]In the notation of the bond activation mechanism, "⇒ *ij*" indicates that the C_i–C_j bond's neighboring bond(s) has been activated, so radical cascade will promote C_i–C_j bond activation; while "; *ij*" indicates none of the C_i–C_j bond's neighboring bond(s) has been activated.

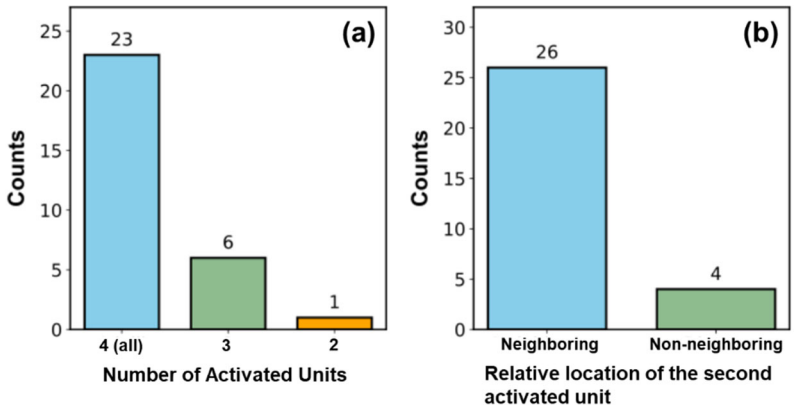

Figure S6. Statistics of the 30 AISMD simulations (**Table S3**). (a) Number of activated benzobarrelane units at the end of the simulation. (b) After the activation of the first benzobarrelane unit, the location of the second unit being activated relative to the first.

Among the 30 AISMD runs within 5 ps, 23 of them resulted in all 4 units being ring-opened, 6 ended up with 3 units opened, and 1 run with 2 units opened (**Fig. S6a**). Among the 23 fully activated tetramer, 21 of them ended up with biradical products, with the 4 cleaving bond lengths and atomic spin densities evolutions plotted in **Fig. S7**. The most important observation is that after all 4 units are activated, all the spin densities are distributed only at the two ends of the activated tetramer (i.e., E_1 and E_8 in **Fig. S5c**), with no spin densities found in the bridging dienes connecting the benzobarrelane units (i.e., B_{23}, B_{45}, and B_{67}). The same evidence can be found in **Fig. S8**, where only 2 or 3 units were activated in the tetramer. Regardless, after all 2 or 3 units are activated, the spin densities are distributed at the two ends of the activated products. Taken Run 24 as an example, after C_3–C_4, C_5–C_6, and C_7–C_8 bonds were sequentially opened, the spin densities are fully distributed at E_8 and B_{23}, where B_{23} can be considered as the end of an activated trimer.

Additionally, we can probe the sequence of tetramer mechanoactivation, particularly the question of after one unit is activated, where is the next activation most likely to occur. 26 out of the 30 cases show that once the first unit is activated, one of its immediately neighboring unit is then activated due to a joint effect of radical cascade and external force (**Fig. S6b**). Taking Run 1 as an example, the bond activation follows the "34 $\Rightarrow$ 56 $\Rightarrow$ 78 $\Rightarrow$ 12" sequence, where after the first C_3–C_4 cleavage, all the remaining 3 units were sequentially activated from the first activated unit following a radical cascade mechanism, suggesting a cooperative activation behavior (**Fig. S7**). Only 4 out of 30 cases, Run 4 (**Fig. S7**), 22, 23, and 30 (**Fig. S9**), showed that after the first unit is activated, a non-neighboring or distant unit is activated next. For example, in Run 4, after bonds C_3–C_4 and C_1–C_2 were cleaved, bond C_7–C_8 were cleaved.

Furthermore, Runs 22, 23, and 30, following the non-neighboring activation sequence, all ended up with tetra-radical products, instead of biradical products (**Fig. S9**). For example, in Run 22, bonds C_3–C_4 and C_1–C_2 break sequentially with a radical cascade reaction, leading to –1 spin density at E_1, and +1 spin density at B_{45}. Before the free radical at B_{45} fragments bond C_5–C_6, bond C_7–C_8 breaks earlier under mechanical force without being facilitated by the generated radicals. The cleavage of C_7–C_8 leads to another pair of free electrons with a –1 spin density at E_8, and +1 spin density at B_{67}. Eventually, this free radical at B_{67} cleaves the C_5–C_6 bond, and that gives an additional up-spin electron in B_{45}, leading to a +2 spin density value there. The other tetra-radical cases show a similar process to Run 22.

All the AISMD calculations support a proposed radical cascade mechanism and cooperative mechanoactivation. After the first bond is mechanochemically cleaved, the biradicals migrate along the backbone bonds connecting the benzobarrelane units, and eventually locate at the end of the ring-opened product.

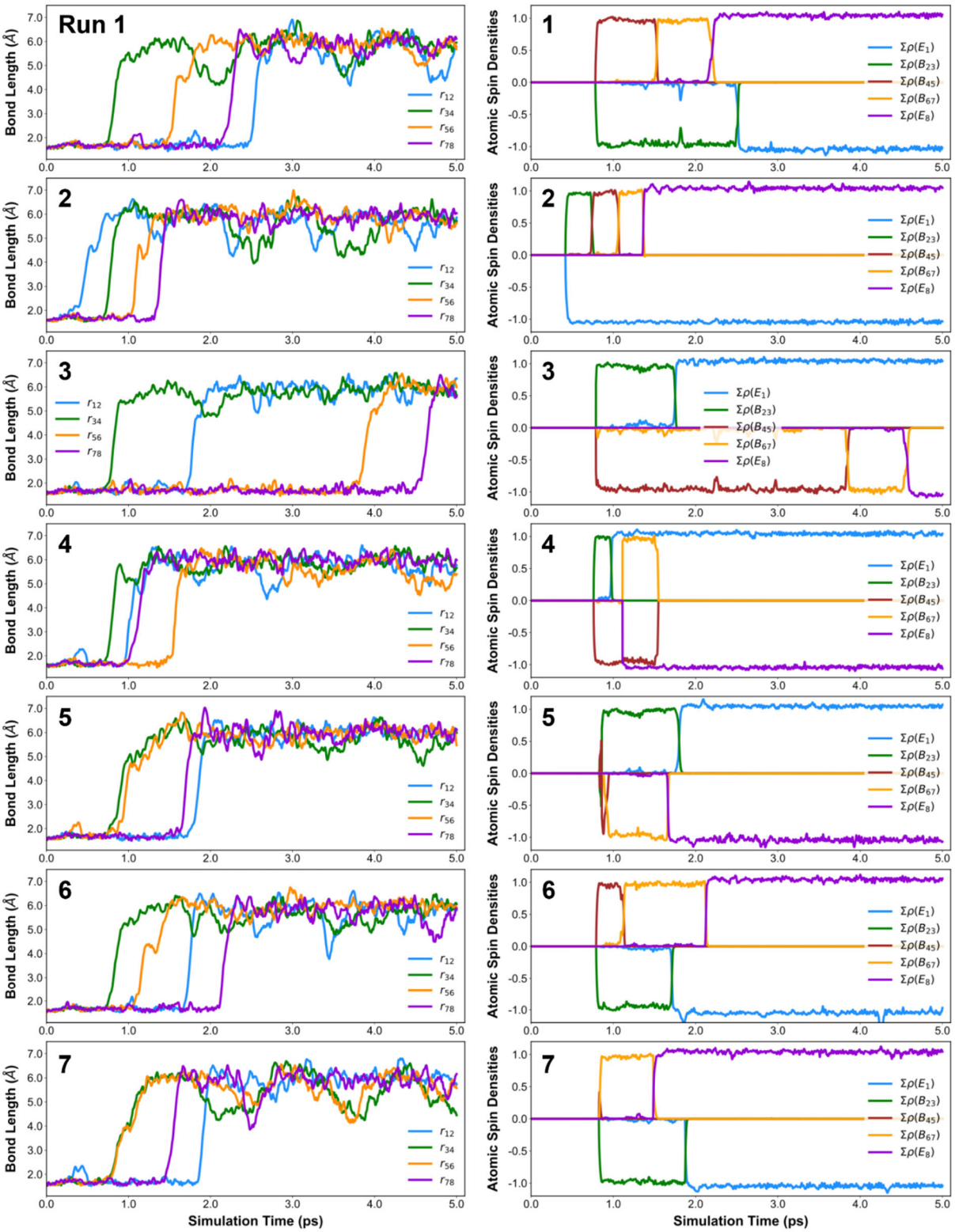

Figure S7. Tetramer AISMD simulations Run 1-7. (Left column) Evolution of the four breaking bond lengths (r_{12}, r_{34}, r_{56}, and r_{78}). (Right column) Evolution of the sum of atomic spin density values at all conjugated dienes, $\Sigma\rho(E_k)$ and $\Sigma\rho(B_{mn})$. **E** denotes a diene at an end of the tetramer, and **B** denotes a bridging diene between two benzobarrelane units. The labels of E_i and B_{jk} are highlighted in (**Fig. S5c**).

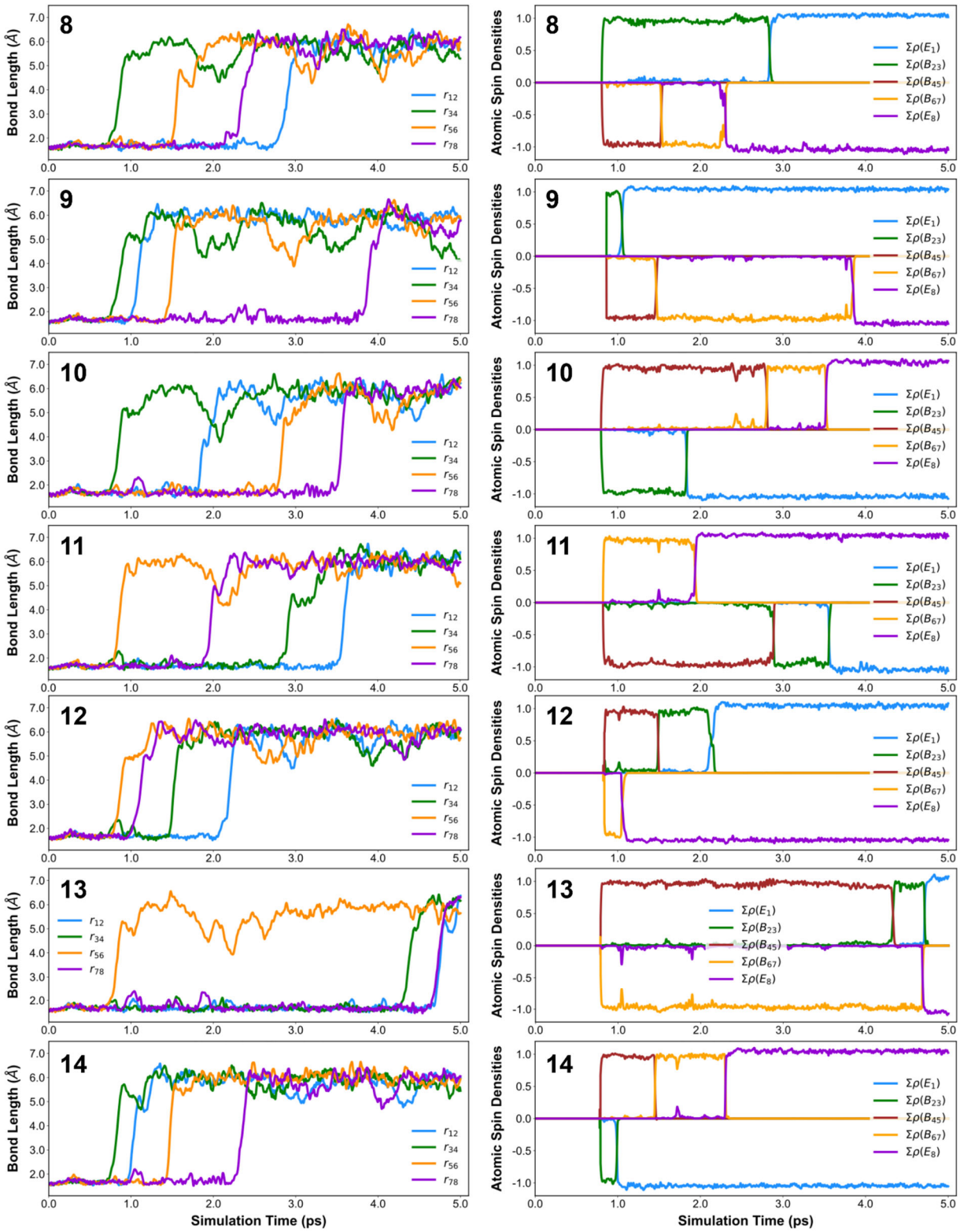

Figure S7. (Cont'd) Tetramer AISMD simulations Run 8-14. (Left column) Evolution of the four breaking bond lengths (r_{12}, r_{34}, r_{56}, and r_{78}). (Right column) Evolution of the sum of atomic spin density values at all conjugated dienes, $\Sigma\rho(E_k)$ and $\Sigma\rho(B_{mn})$. **E** denotes a diene at an end of the tetramer, and **B** denotes a bridging diene between two benzobarrelane units. The labels of E_i and B_{jk} are highlighted in (**Fig. S5c**).

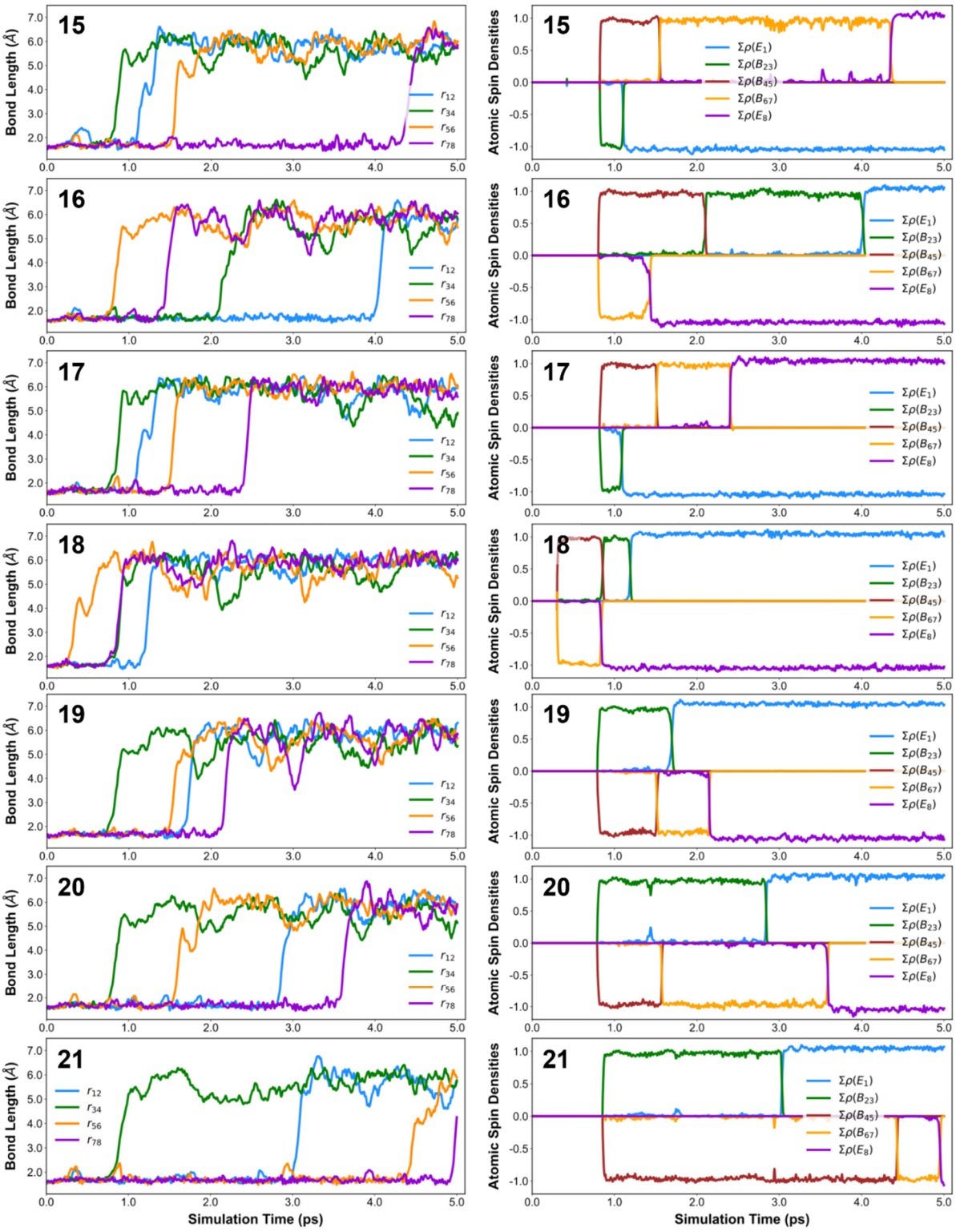

Figure S7. (Cont'd) Tetramer AISMD simulations Run 15-21. (Left column) Evolution of the four breaking bond lengths (r_{12}, r_{34}, r_{56}, and r_{78}). (Right column) Evolution of the sum of atomic spin density values at all conjugated dienes, $\Sigma\rho(E_k)$ and $\Sigma\rho(B_{mn})$. **E** denotes a diene at an end of the tetramer, and **B** denotes a bridging diene between two benzobarrelane units. The labels of E_i and B_{jk} are highlighted in (**Fig. S5c**).

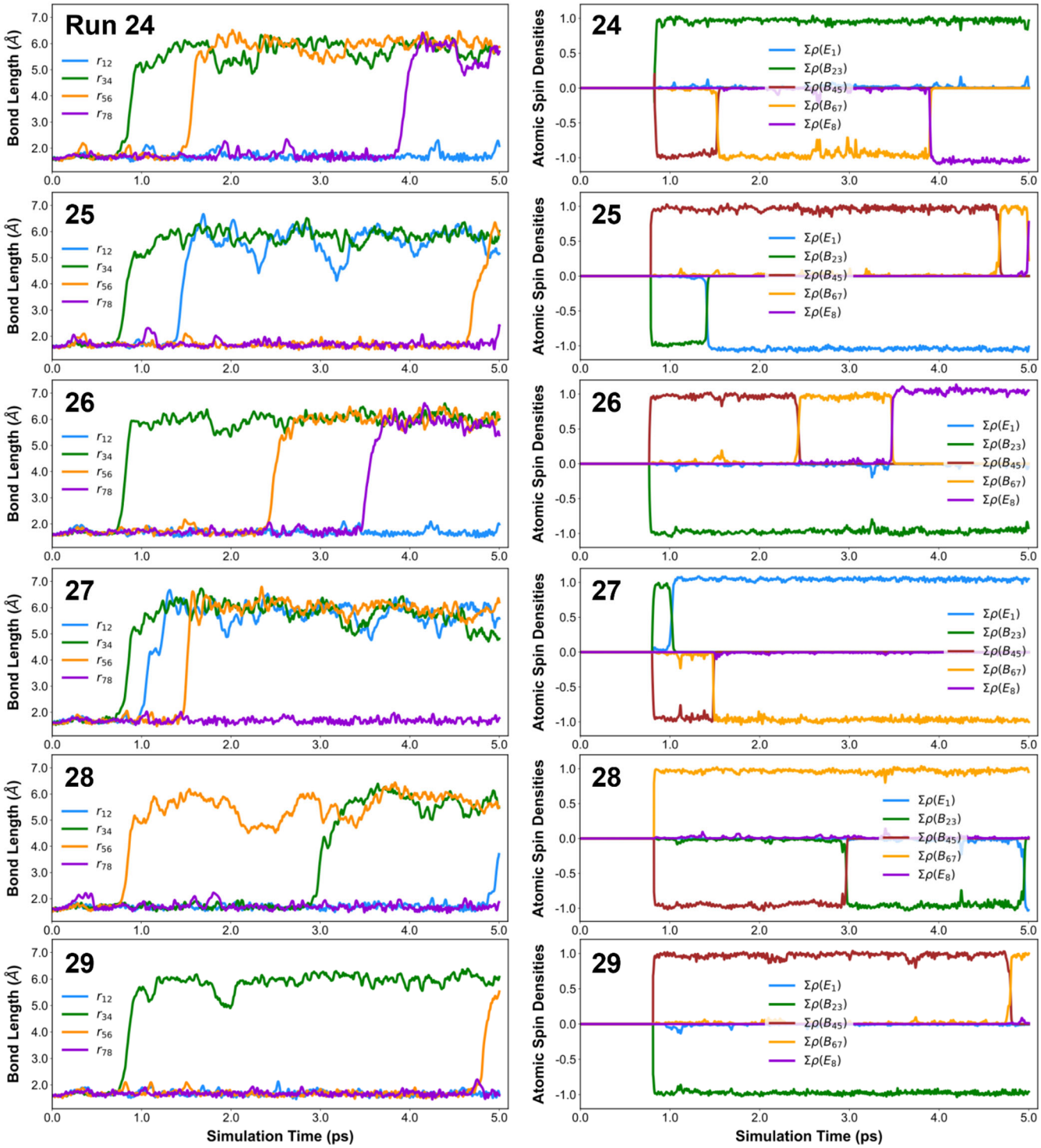

Figure S8. Tetramer AISMD simulations Run 24-29, in which not all four bonds were activated. (Left column) Evolution of the four breaking bond lengths (r_{12}, r_{34}, r_{56}, and r_{78}). (Right column) Evolution of the sum of atomic spin density values at all conjugated dienes, $\Sigma\rho(E_k)$ and $\Sigma\rho(B_{mn})$. **E** denotes a diene at an end of the tetramer, and **B** denotes a bridging diene between two benzobarrelane units. The labels of E_i and B_{jk} are highlighted in (**Fig. S5c**).

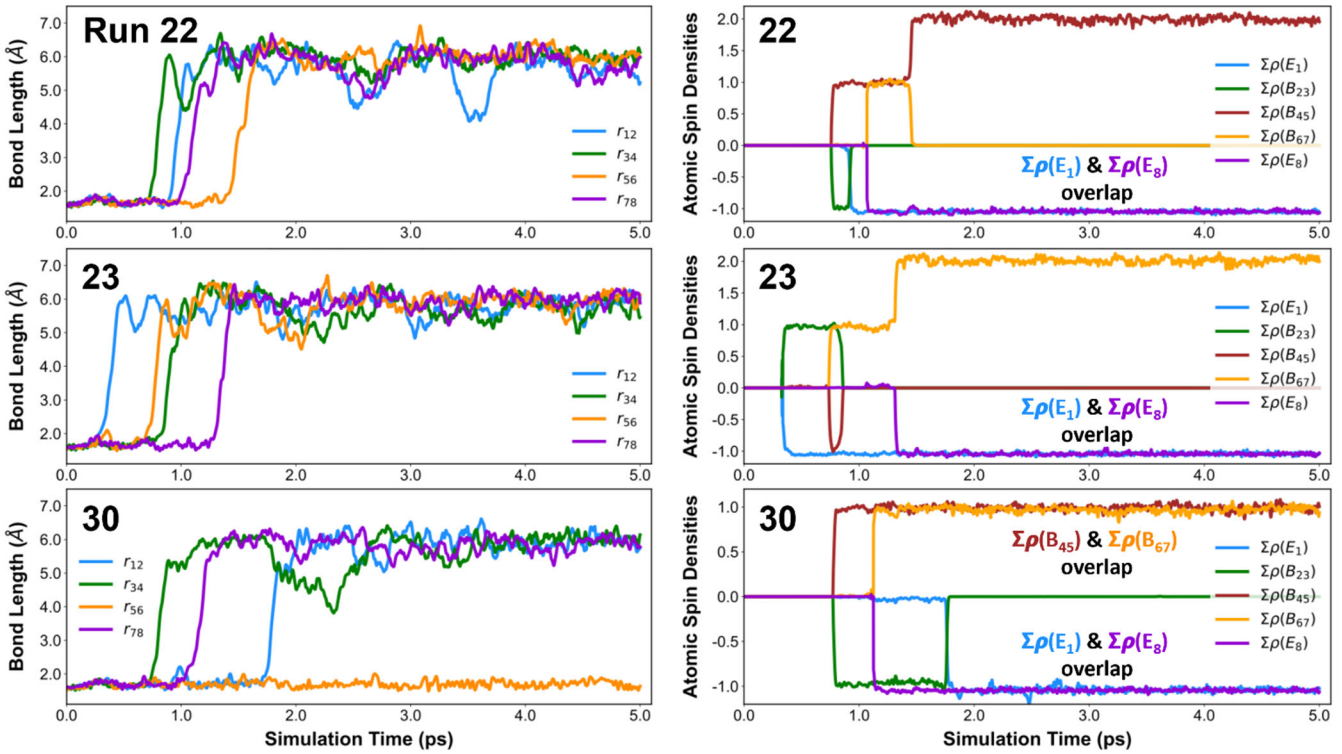

Figure S9. Tetramer AISMD simulations Run 22, 23, and 30, in which the tetra-radicals were formed as the activated product. (Left column) Evolution of the four breaking bond lengths (r_{12}, r_{34}, r_{56}, and r_{78}). (Right column) Evolution of the sum of atomic spin density values at all conjugated dienes, $\Sigma\rho(E_k)$ and $\Sigma\rho(B_{mn})$. **E** denotes a diene at an end of the tetramer, and **B** denotes a bridging diene between two benzobarrelane units. The labels of E_i and B_{jk} are highlighted in (**Fig. S5c**).

S6.3. Dimer system – Force modified potential energy surface and microkinetic modeling

We investigated the force-modified potential energy surface (FMPES),[9] electronic structures, and kinetic rates of the radical cascade mechanism. We focused on the mechanoactivation of a dimeric structure **2**, which is the minimum necessary unit for probing the formation of mechanochemical product **4** via intermediate **3** (**Fig. S10a**). A *cis* alkene was used for calculation of **2**. We calculated the FMPES of the mechanoactivation at force levels f = 0.5, 1.0, 1.5, 2.0, and 2.5 nN using the same UB3LYP-D3/6-31G* level of theory. The optimized structures of reactant **2**, intermediate **3**, and product **4** at the five force levels are shown as clusters in **Fig. S10b**. The same critical geometries, transition states, and potential energy values were also computed for the force-free (i.e., f = 0 nN) case.

For the dimer system, two critical reaction steps are found on the FMPES: the first bond cleavage in reactant **2** to form the biradical intermediate **3**, where the linkage displays a pro-*cis*-ene structure. We refer to this intermediate as **3-*cis***. The pro-*cis*-ene structure can isomerize into a pro-*trans*-ene structure, which we refer to **3-*trans***. The **3-*trans*** structure is followed by cleavage of the second bond to form

product **4** with a diene linkage. The reaction paths of the first and second bond cleavage reactions, represented as the intrinsic reaction coordinates (IRCs) are shown in **Fig. 6b** in the main text.

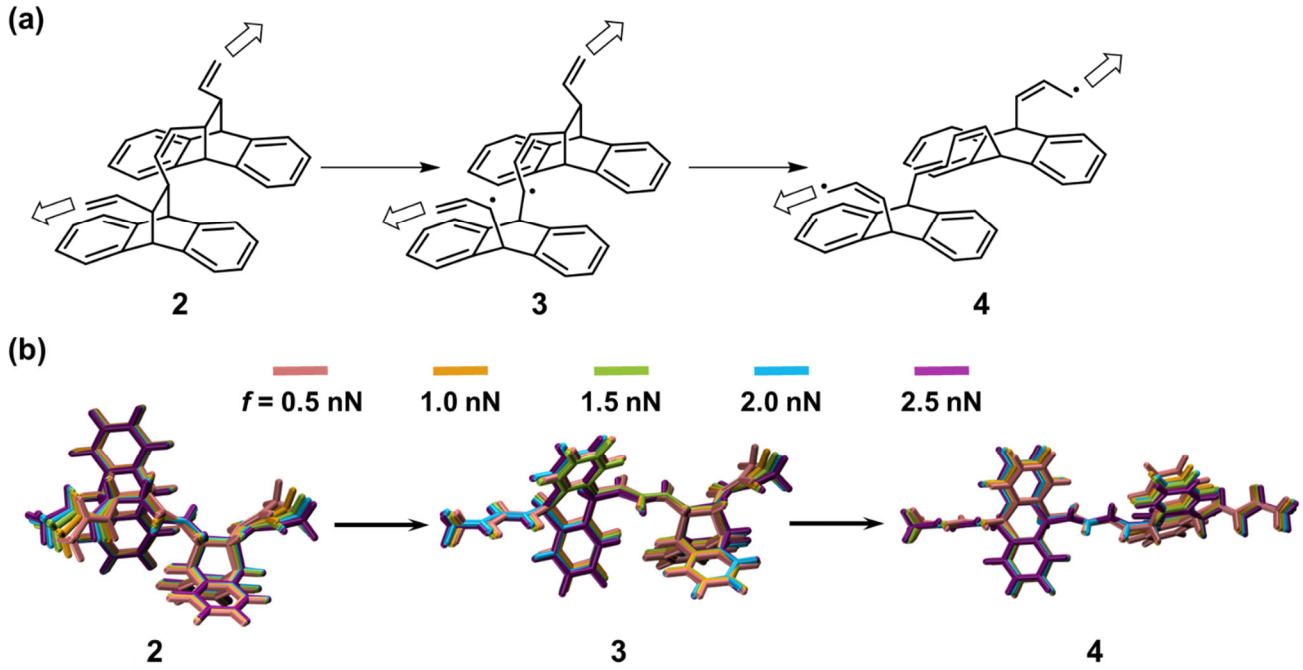

Figure S10. **(a)** The proposed mechanoactivation mechanism of a dimeric benzobarrelane system. **(b)** The optimized geometry structures of the dimer reactant **2**, intermediate **3** (the *trans*-isomer), and activated dimer product **4**, under external forces at five levels. The geometry structures are aligned and clustered.

Figure S11 shows the force-modified potential energies of all the critical geometries, including Reactant **2**, Intermediate **3-*cis***, Intermediate **3-*trans***, and Product **4**, along with the transition state structures of the first bond cleavage ($TS_{2\text{-}3}$), the second bond cleavage ($TS_{3\text{-}4}$), and the isomerization between **3-*cis*** and **3-*trans*** ($TS_{cis\text{-}trans}$). At each force level, the energy values are referenced as zero at the reactant. The bottom table in **Fig. S11** shows the corresponding energy values in the force modified potential energy diagram. The values in the parentheses are transition state barrier heights (i.e.., for $TS_{2\text{-}3}$, the values in the parenthesis are obtained by $E_{3\text{-}cis} - E_2$; for $TS_{cis\text{-}trans}$, $E_{3\text{-}trans} - E_{3\text{-}cis}$; and for $TS_{3\text{-}4}$, $E_4 - E_{3\text{-}trans}$). For the first and second bond cleavage steps, as the external force is increased, the activation energies are lowered with the transition state occurring earlier towards the reactants. Furthermore, under the same external force, the barrier heights of two reaction steps are found to be similar, which could imply similar kinetic rates of C–C bond cleavage. Lastly, the barriers of **3-*cis*** and **3-*trans*** isomerization are consistently lower than the barriers of the two bond cleavage reactions, indicating that isomerization reaction is not rate limiting. Alternative paths, e.g., cleaving the first bond from **2** to **3-*cis***, and cleaving

the second bond from **3-*trans*** to **4** should exist, and the barrier heights should be similar to those of the existing two bond cleavage reactions. Therefore, we do not exhaust the search on the alternative paths. The energy information, including electronic energy, force-modified potential energy, and Gibbs free energy of all the critical geometries at multiple force levels are listed in **Table S4**.

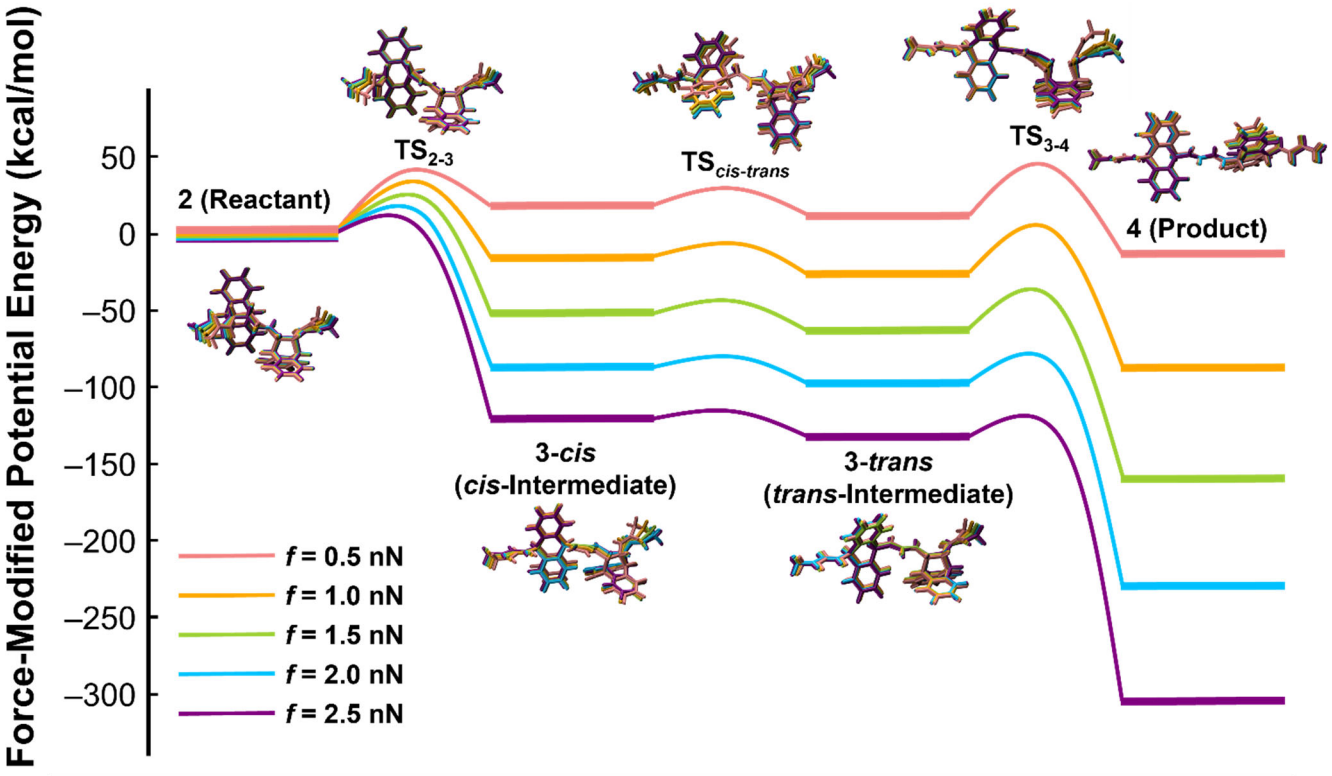

	Force-Modified Potential Energy (kcal/mol)						
Force	**2**	**TS_{2-3}**	**3-*cis***	**$TS_{cis-trans}$**	**3-*trans***	**TS_{3-4}**	**4**
***f* = 0.5 nN**	0.0	41.8 (41.8)	18.5	30.5 (12.0)	11.2	46.4 (35.2)	–13.2
***f* = 1.0 nN**	0.0	34.2 (34.2)	–16.0	–6.4 (9.6)	–26.6	5.6 (32.2)	–87.6
***f* = 1.5 nN**	0.0	26.0 (26.0)	–51.9	–43.2 (8.7)	–63.0	–36.5 (26.5)	–159.4
***f* = 2.0 nN**	0.0	18.3 (18.3)	–87.1	–79.2 (7.9)	–97.7	–78.0 (19.7)	–229.8
***f* = 2.5 nN**	0.0	11.3 (11.3)	–120.7	–114.3 (6.4)	–132.1	–118.4 (13.7)	305.3

Figure S11. Force modified potential energy diagram of all the critical geometries along the mechanochemical activation pathway. These geometries are Reactant (**2**), TS_{2-3}, *cis*-Intermediate (**3-*cis***), $TS_{cis-trans}$, *trans*-Intermediate (**3-*trans***), TS_{3-4}, Product (**4**). At each force level, the energy values are referenced as zero at the reactant. For each critical geometry, the optimized structures at all five force

levels are aligned and clustered. The bottom table shows the corresponding values in the force modified potential energy diagram. The values in the parentheses are transition state barrier heights (i.e.., for $TS_{2\text{-}3}$, the values in the parenthesis are obtained by $E_{\mathbf{3}\text{-}cis} - E_{\mathbf{2}}$; for $TS_{cis\text{-}trans}$, $E_{\mathbf{3}\text{-}trans} - E_{\mathbf{3}\text{-}cis}$; and for $TS_{3\text{-}4}$, $E_{\mathbf{4}} - E_{\mathbf{3}\text{-}trans}$).

Table S4. Electronic energy E_{elec}, Force-Modified Potential Energy E_{FMPE}, and Gibbs free energy, G (at 298 K) for all the critical geometries and transition states calculated at force free (f = 0 nN) and five force-applied conditions (f = 0.5, 1.0, 1.5, 2.0, and 2.5 nN). Energy units: Hartree.

	2	**$TS_{2\text{-}3}$**	**3-*cis***	**$TS_{cis\text{-}trans}$**	**3-*trans***	**$TS_{3\text{-}4}$**	**4**
f = 0 nN							
E_{elec}	–1546.10641	N/A	–1546.03083	–1545.99698	–1546.02629	–1545.99192	–1546.00262
E_{FMPE}	–1546.10641	N/A	–1546.03083	–1545.99698	–1546.02629	–1545.99192	–1546.00262
G	–1545.51721	N/A	–1545.45074	–1545.41809	–1545.44578	–1545.41615	–1545.42756
f = 0.5 nN							
E_{elec}	–1546.09680	–1546.01974	–1546.01636	–1545.98895	–1546.01668	–1545.96234	–1545.99501
E_{FMPE}	–1546.22891	–1546.16235	–1546.19946	–1546.18036	–1546.21103	–1546.15503	–1546.25014
G	–1545.64203	–1545.58074	–1545.62060	–1545.60166	–1545.63251	–1545.57954	–1545.67563
f = 1.0 nN							
E_{elec}	–1546.08262	–1546.00234	–1545.99787	–1545.97431	–1546.00714	–1545.93898	–1545.98766
E_{FMPE}	–1546.36611	–1546.31169	–1546.39162	–1546.37628	–1546.40855	–1546.35715	–1546.50572
G	–1545.77952	–1545.72971	–1545.81350	–1545.79904	–1545.83076	–1545.78274	–1545.93224
f = 1.5 nN							
E_{elec}	–1546.06468	–1545.98551	–1545.97940	–1545.95963	–1545.99496	–1545.92295	–1545.97862
E_{FMPE}	–1546.51151	–1546.47005	–1546.59425	–1546.58038	–1546.61183	–1546.56970	–1546.76554
G	–1545.92606	–1545.88795	–1546.01672	–1546.00420	–1546.03513	–1545.99581	–1546.19290
f = 2.0 nN							
E_{elec}	–1546.04368	–1545.96765	–1545.96061	–1545.94322	–1545.97802	–1545.90720	–1545.96788
E_{FMPE}	–1546.66359	–1546.63442	–1546.80245	–1546.78975	–1546.81924	–1546.78785	–1547.02986
G	–1546.07878	–1546.05293	–1546.22571	–1546.21357	–1546.24344	–1546.21479	–1546.45835
f = 2.5 nN							
E_{elec}	–1546.02078	–1545.94977	–1545.93819	–1545.92653	–1545.95986	–1545.89251	–1545.95925
E_{FMPE}	–1546.82114	–1546.80314	–1547.01355	–1547.00325	–1547.03162	–1547.00982	–1547.30769
G	–1546.23735	–1546.22262	–1546.43848	–1546.42803	–1546.45657	–1546.43753	–1546.73739

Using the potential and free energy information, we further performed microkinetic modeling considering all the possible elementary reactions and their respective kinetic rates. Under each external force (f = 0.5, 1.0, 1.5, 2.0, and 2.5 nN), we model the kinetic evolution of the dimer mechanochemical activation with the following elementary reactions.

$$\mathbf{2} \underset{k_{1b}}{\overset{k_{1f}}{\rightleftharpoons}} \mathbf{3}\text{-}cis$$

$$\mathbf{3}\text{-}cis \underset{k_{2b}}{\overset{k_{2f}}{\rightleftharpoons}} \mathbf{3}\text{-}trans$$

$$\mathbf{3}\text{-}trans \underset{k_{3b}}{\overset{k_{3f}}{\rightleftharpoons}} \mathbf{4}$$

The forward and backward reaction rates are calculated using transition state theory,[16-18] given by

$$k_f = \frac{k_B T}{h} e^{-\Delta G_f^{\ddagger}/RT}$$
$$k_b = \frac{k_B T}{h} e^{-\Delta G_b^{\ddagger}/RT}$$

where k_B is the Boltzmann constant, h is the Planck constant, $\Delta G_f^{\ddagger}$ is the difference of standard Gibbs free energy of the transition state and the reactant, and $\Delta G_b^{\ddagger}$ is the Gibbs free energy difference between the transition and the product. To compute the free energy of the respective stationary points, the rigid-rotor approximation was used in combination with a modified harmonic approximation, where small vibrational frequencies below 100 cm^{-1} were scaled to this value in order to avoid divergence of the entropic contribution of low-frequency modes.

Microkinetic modeling is performed at constant temperature at $T = 298$ K, by solving the following system ordinary differential equations (ODEs)

$$\frac{d}{dt}\begin{bmatrix} X_{\mathbf{2}} \\ X_{\mathbf{3}\text{-}cis} \\ X_{\mathbf{3}\text{-}trans} \\ X_{\mathbf{4}} \end{bmatrix} = \begin{bmatrix} -k_{1f} & k_{1b} & 0 & 0 \\ k_{1f} & -k_{1b}-k_{2f} & k_{2b} & 0 \\ 0 & k_{2f} & -k_{2b}-k_{3f} & k_{3b} \\ 0 & 0 & k_{3f} & -k_{3b} \end{bmatrix} \begin{bmatrix} X_{\mathbf{2}} \\ X_{\mathbf{3}\text{-}cis} \\ X_{\mathbf{3}\text{-}trans} \\ X_{\mathbf{4}} \end{bmatrix}$$

where $X_{\mathbf{2}}$, $X_{\mathbf{3}\text{-}cis}$, $X_{\mathbf{3}\text{-}trans}$, and $X_{\mathbf{4}}$ are the mole fractions to be solved. Since the reaction rate coefficients, k, can differ by several orders of magnitude, this ODE system is very stiff. We used backward differentiation formula (BDF) for numerical integration, which guarantees the stability of the stiff-ODE solutions. Under each external force, the initial condition starts with 100% Reactant **2** (i.e., $X_{\mathbf{2}} = 1.0$), and the modeling is performed at constant $T = 298$ K.

Figure S12 shows the microkinetic modeling results under the external force $f = 1.0$, 1.5, 2.0, and 2.5 nN (the result of 0.5 nN was not shown since the time scale is exceptionally long). As the external force is raised in each 0.5 nN increment, the mechanoactivation time scale of the dimer drops dramatically by orders of magnitude, i.e., from $O(10^{10}$ s) at $f = 1.0$ nN, to $O(10^{6}$ s) at $f = 1.5$ nN, $O(10^{0}$ s) at $f = 2.0$ nN, and $O(10^{-4}$ s) at $f = 2.5$ nN. Clearly, this decrease of reaction time scale is due to the lowering of the ring-opening barrier by increasing applied force (**Fig. S11**). Furthermore, the reaction time scale of the first and second bond activation can be approximated as the lifetime of Reactant **2** and Intermediate **3**, respectively. As the force increases above 1.5 nN, the second bond activation requires slightly longer time compared to the first bond activation, due to slightly higher reaction barrier of $TS_{3\text{-}4}$ than $TS_{2\text{-}3}$ (**Fig. S11**

table). The slightly higher barrier of $TS_{3\text{-}4}$ can be explained by a catch-bond behavior. According to the CASSCF natural orbital contours (**Fig. S13-S17**), as force increases, the π-electrons in the $TS_{3\text{-}4}$ bridge diene are less favorable to migrate towards the second breaking bond, due to a misalignment between the π-electrons and the breaking bond. Nevertheless, this effect of $TS_{3\text{-}4}$ is insignificant compared to the drastically lowered barriers of the two sequential bond opening reactions at large external forces.

Furthermore, as external force increases, the intermediate **3** can be stabilized after the first bond cleavage, as its mole fraction gradually increases as force increases (**Fig. S12**). Two major reasons give rise to this stabilization: 1) the lower reaction barrier of the first bond cleavage; 2) the lower *cis*-*trans* isomerization barrier than the two bond breaking barriers. Thus, rapid isomerization between *cis*- and *trans*-isomers extends the lifetime of the intermediate structure.

We further computed electron density distribution on the natural orbital contours of the critical geometries, which can also support the mechanism of radical cascade mechanoactivation. **Figure S13-S17** displays the two singly occupied molecular orbitals (SOMOs) of the critical geometries along the reaction coordinate (i.e., **2**, $TS_{2\text{-}3}$, **3-*cis***, $TS_{cis\text{-}trans}$, **3-*trans***, $TS_{3\text{-}4}$, and **4**) at all five force levels, respectively. The natural orbital contours are obtained with single-point energy calculations at CAS(2,2)SCF/6-31G* level of theory. As consistently observed through Figs. **S13-S17**, the transition state of the first ring-opening reaction ($TS_{2\text{-}3}$) exhibits *σ*-bond cleavage that creates the biradical intermediate **3-*cis*** and **3-*trans***. In the second ring-opening transition state structure ($TS_{3\text{-}4}$), the biradicals migrate towards opposite directions on the backbone through π-orbitals. In product **4**, the electrons are localized at the ends of the dimer.

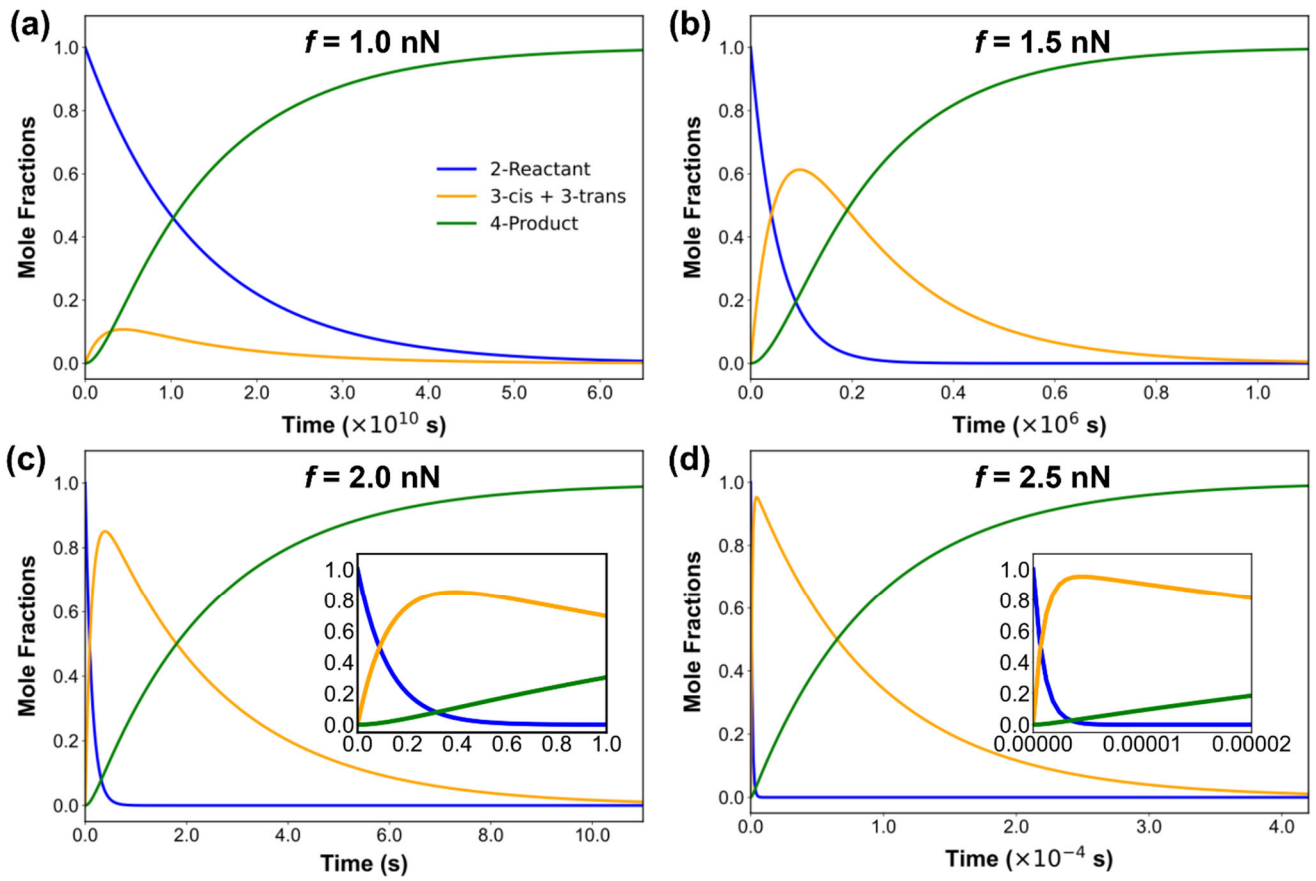

Figure S12. Microkinetic modeling results for mechanoactivation of the benzobarrelane dimer under **(a)** f = 1.0 nN, **(b)** f = 1.5 nN, **(c)** f = 2.0 nN, and **(d)** f = 2.5 nN. The mole fraction evolution of **2**, **3** (including both **3-*cis*** and **3-*trans***) and **4** are plotted as a function of reaction time. Insets in panel (c) and (d) are the zoomed-in plots for the initial evolution of the model system.

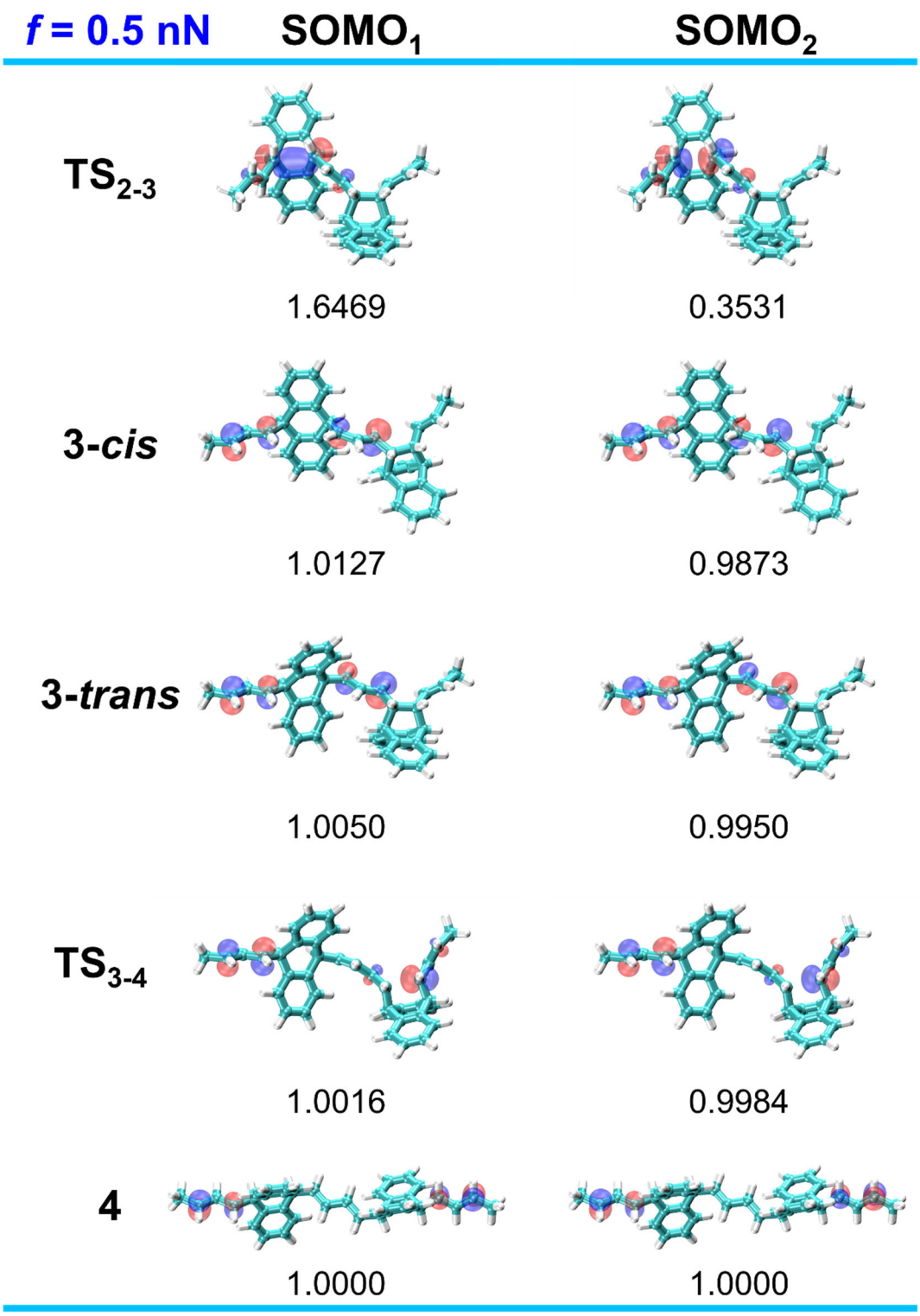

Figure S13. Natural orbital contours of two singly occupied molecular orbitals (SOMOs) obtained from CAS(2,2)SCF/6-31G* single-point calculations on $TS_{2\text{-}3}$, intermediate **3-*cis***, intermediate **3-*trans***, $TS_{3\text{-}4}$, and Product **4** configurations at 0.5 nN force. Occupation numbers are shown at the bottom of each orbital.

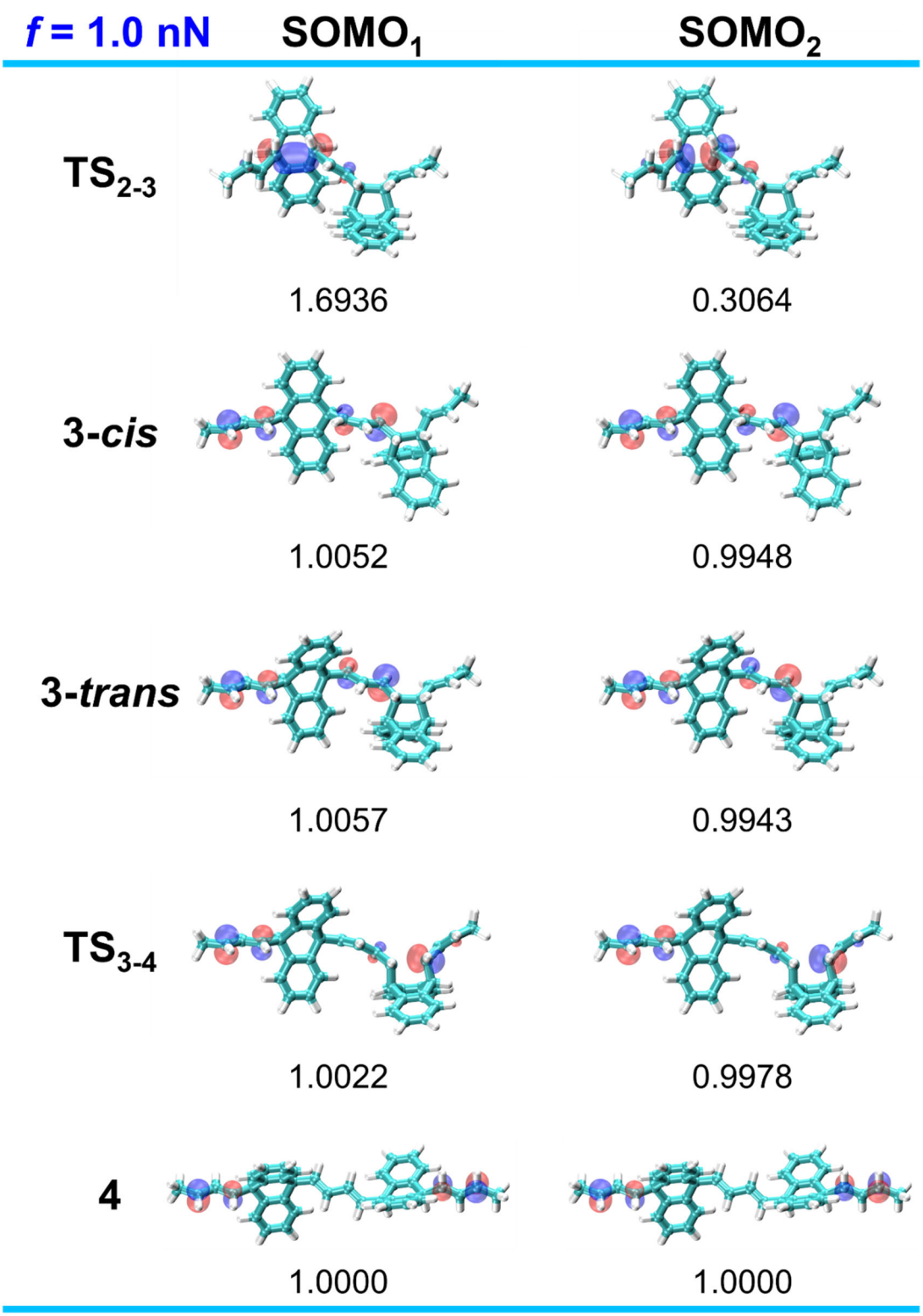

Figure S14. Natural orbital contours of two singly occupied molecular orbitals (SOMOs) obtained from CAS(2,2)SCF/6-31G* single-point calculations on $TS_{2\text{-}3}$, intermediate **3-*cis***, intermediate **3-*trans***, $TS_{3\text{-}4}$, and Product **4** configurations at 1.0 nN force. Occupation numbers are shown at the bottom of each orbital.

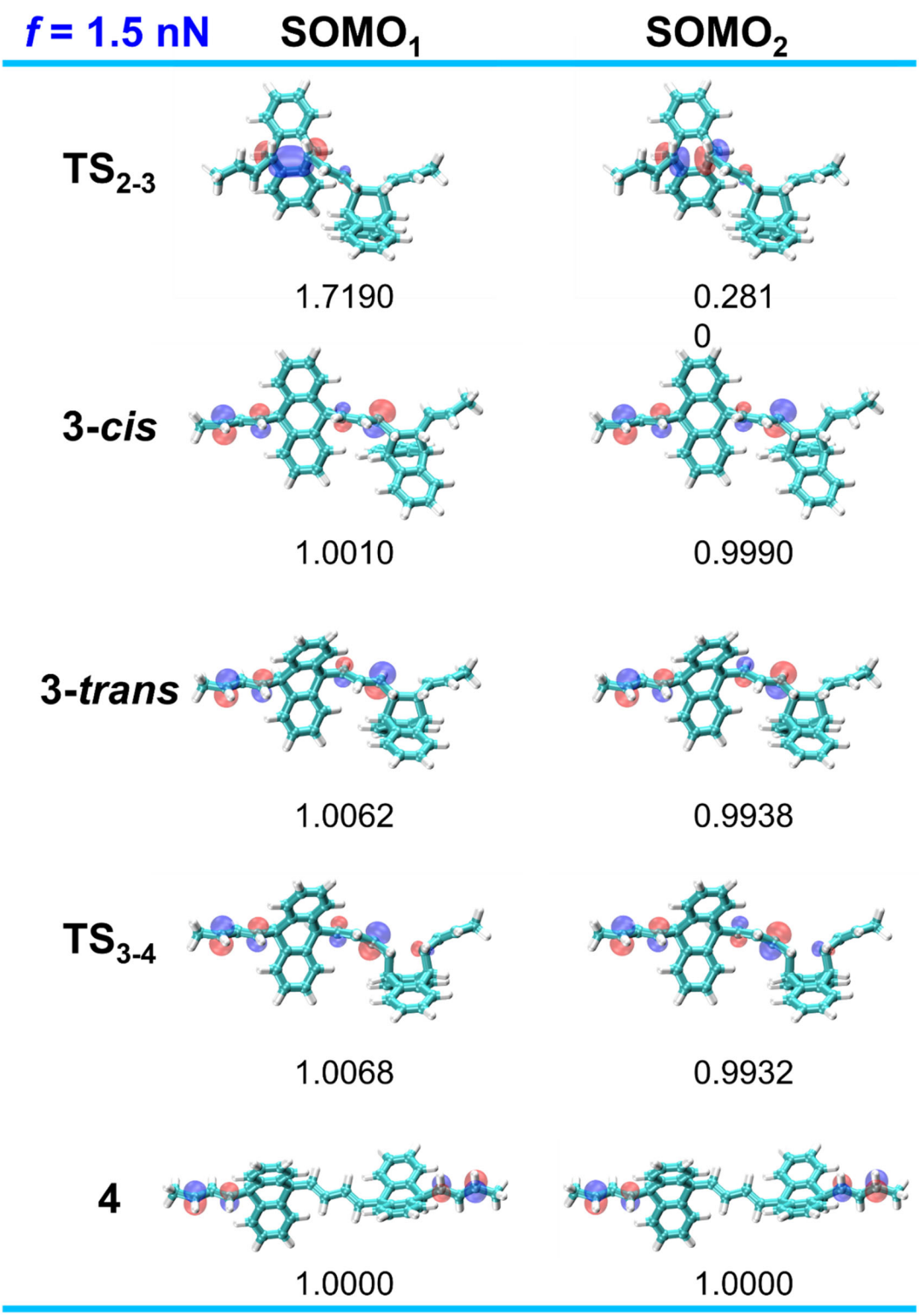

Figure S15. Natural orbital contours of two singly occupied molecular orbitals (SOMOs) obtained from CAS(2,2)SCF/6-31G* single-point calculations on $TS_{2\text{-}3}$, intermediate **3-*cis***, intermediate **3-*trans***, $TS_{3\text{-}4}$, and Product **4** configurations at 1.5 nN force. Occupation numbers are shown at the bottom of each orbital.

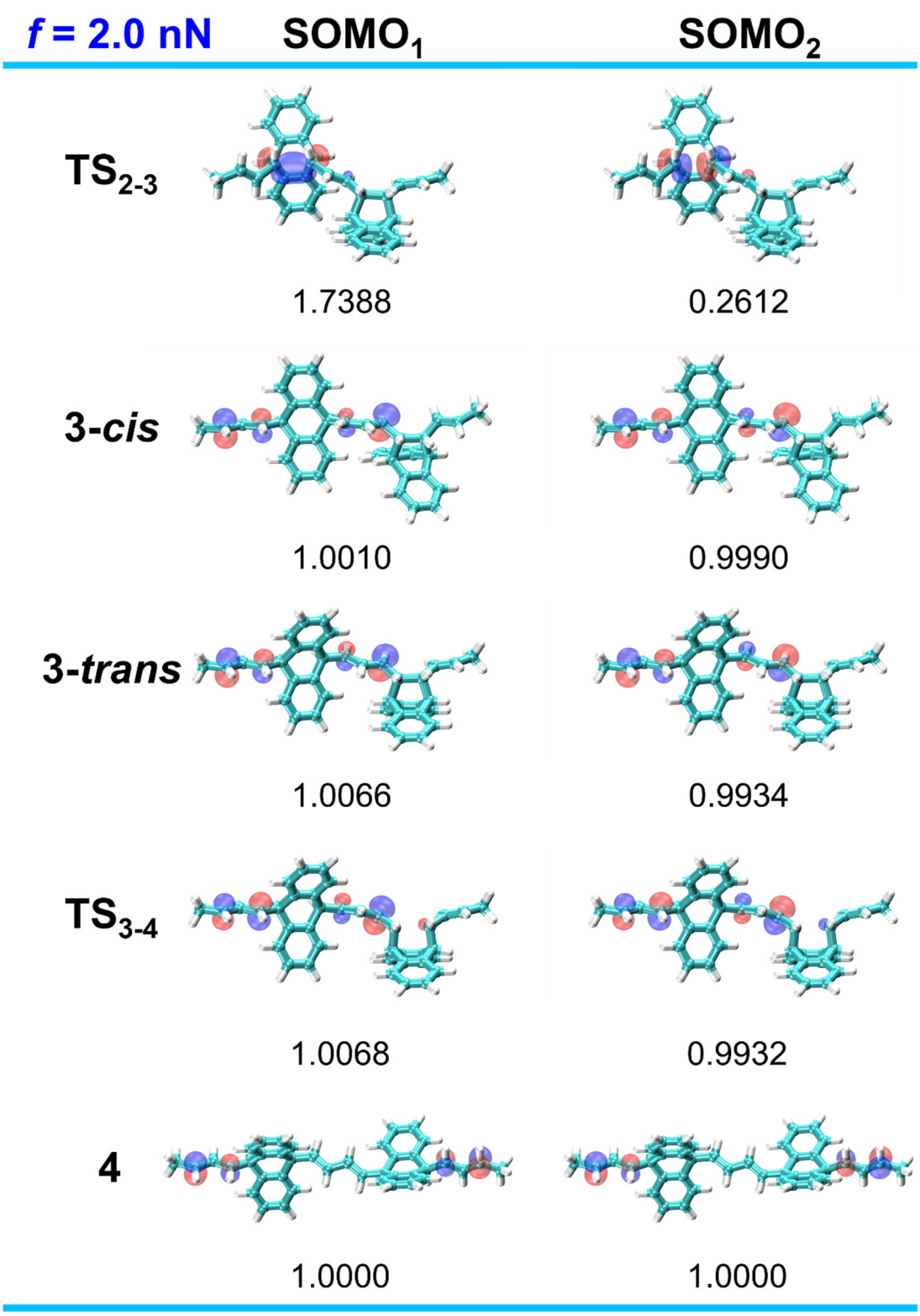

Figure S16. Natural orbital contours of two singly occupied molecular orbitals (SOMOs) obtained from CAS(2,2)SCF/6-31G* single-point calculations on $TS_{2\text{-}3}$, intermediate **3-*cis***, intermediate **3-*trans***, $TS_{3\text{-}4}$, and Product **4** configurations at 2.0 nN force. Occupation numbers are shown at the bottom of each orbital.

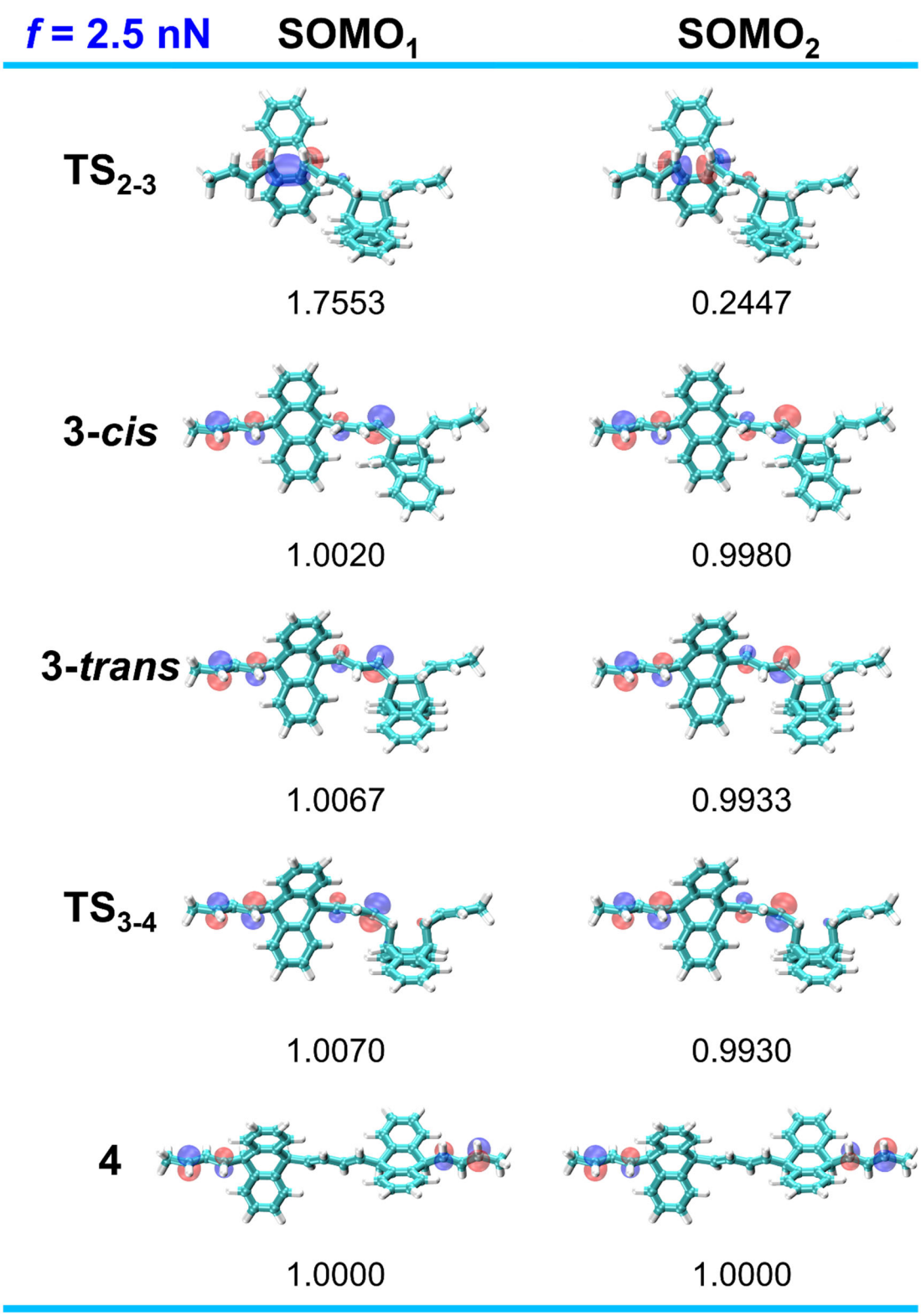

Figure S17. Natural orbital contours of two singly occupied molecular orbitals (SOMOs) obtained from CAS(2,2)SCF/6-31G* single-point calculations on $TS_{2\text{-}3}$, intermediate **3-*cis***, intermediate **3-*trans***, $TS_{3\text{-}4}$, and Product **4** configurations at 2.5 nN force. Occupation numbers are shown at the bottom of each orbital.

S6.4 Ring strain calculation

Ring strain calculations were done by simulating a ring opening reaction of the benzobarrelane unit. The geometry of each molecule was optimized to yield a minimum energy. To account for the change in the number of hydrogens and the change in hybridization of the carbons, additional molecules were optimized to add to either side (**Fig. S25**). Optimizations to an energy minimum done in Gaussian 16[19] using RB3LYP/6-31G* level of theory. The molecules were chosen to satisfy homodesmotic criteria (**Table S5**) to minimize error in calculation.[20]

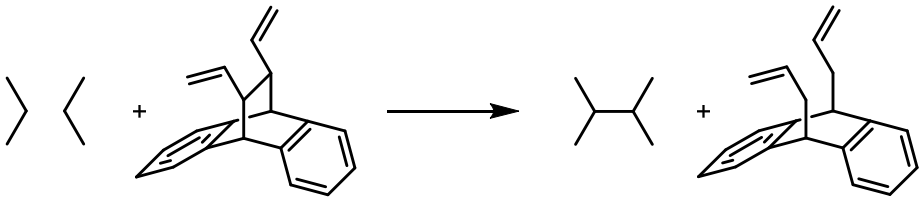

Figure S18. Reaction and molecules considered for the benzobarrelane ring strain calculation.

Table S5. Summary of the Homodesmotic analysis

Homodesmotic Analysis	Left Side	Right Side
CH_3 (sp^3)	4	4
CH_2 (sp^3)	2	2
CH (sp^3)	4	4
CH_2 (sp^2)	2	2
CH (sp^2)	10	10
C (sp^2)	4	4

Table S6. Energies calculated for each species in the ring strain calculation

Species	Energy (kcal/mol)
Propane	-74763
Benzobarrelane	-485006.66
2,3-dimethylbutane	-148769.25
Benzobarrelane (Open)	-485773.105
Energy Difference	9.67

Using the energy values in **Table S6**, the ring strain energy can be calculated as follows.

$$Ring\ Strain = (2 * Propane + Barrelane) - (Dimethylbutane + Open\ Barrelane)$$
$$= \big(2 * (-74763) + (-485006.66)\big) - \big((-148769.25) + (-485773.105)\big)$$
$$= 9.67\ kcal/mol$$

S6.5 Contour length calculation

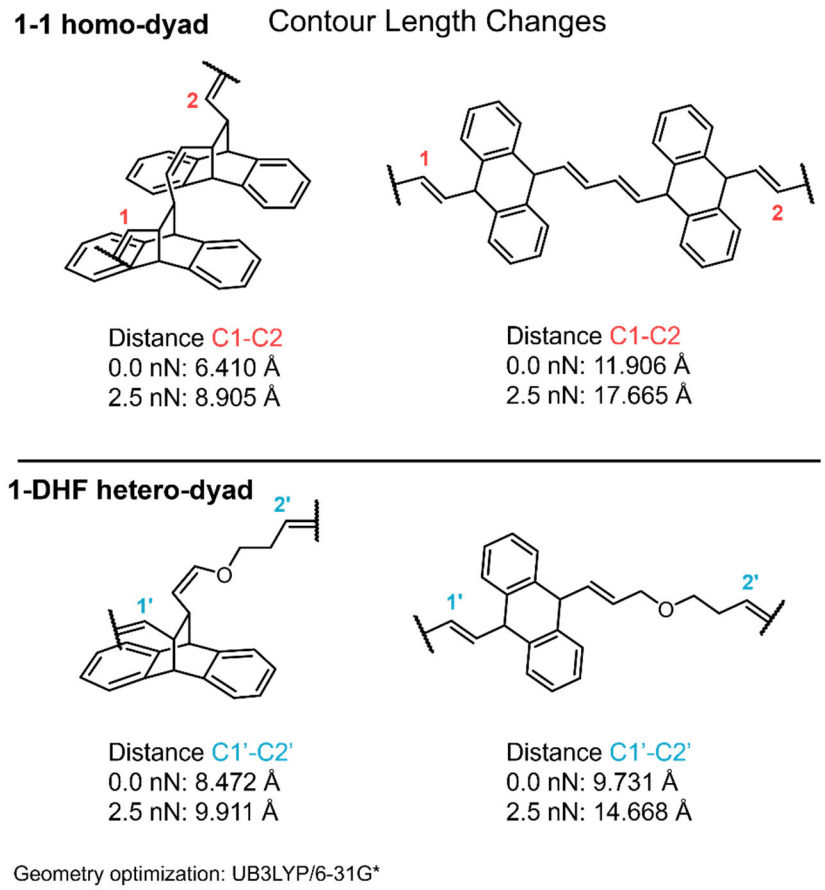

Figure S19. Computed contour length for benzobarrelane-benzobarrelane homo-dyad under 0.0 nN and 2.5 nN and benzobarrelane-DHF hetero-dyad under 0.0 nN and 2.5 nN.

S7. Movie files of AISMD simulations

Movie 1: Tetramer_AISMD_Run8_Fig5f
AISMD simulation for tetramer ring-opening (used for **Fig. 5**). Bond cleavage starts from an internal benzobarrelane unit with the bond cleavage sequence 34 => 56 => 78 => 12. The bond labeling convention is defined in Fig. 5a. Bond length evolutions are simultaneously played for reference.

Movie 2: Movie2_Tetramer_AISMD_Run2_FigS7
AISMD simulation for tetramer ring-opening (used for **Fig. S7**). Bond cleavage starts from a terminal benzobarrelane unit with the bond cleavage sequence 12 => 34 => 56 => 78. The bond labeling convention is defined in Fig. 5a. Bond length evolutions are simultaneously played for reference.

References

1. Çapan, İ.; Servi, S.; Dalkılıç, S.; Dalkılıç, L. K., Synthesis and Anticancer Evaluation of Benzimidazole Derivatives Having Norbornene/Dibenzobarrelene Skeletons and Different Functional Groups. *ChemistrySelect* **2020,** *5* (45), 14393-14398.
2. Weber, E.; Csoeregh, I.; Ahrendt, J.; Finge, S.; Czugler, M., Design of roof-shaped clathrate hosts. Inclusion properties and x-ray crystal structures of a free host and of inclusion compounds with 1-butenol and DMF. *J. Org. Chem.* **1988,** *53* (25), 5831-5839.
3. Weinges, K.; Sipos, W.; Klein, J.; Deuter, J.; Irngartinger, H., Kondensierte Ringsysteme, XVIII Zur Synthese von Cyclobuten-Derivaten aus den entsprechenden Thiolanen – Kristall- und Molekülstruktur von 2,5-o-Benzeno-3,4-benzo[4.2.2]propella-3,7,9-trien. *Chem. Ber.* **1987,** *120* (1), 5-9.
4. Havare, N.; Plattner, D. A., Oxidative Cleavage of α-Aryl Aldehydes Using Iodosylbenzene. *Org. Lett.* **2012,** *14* (19), 5078-5081.
5. Ufimtsev, I. S.; Martínez, T. J., Quantum Chemistry on Graphical Processing Units. 1. Strategies for Two-Electron Integral Evaluation. *J. Chem. Theory Comput.* **2008,** *4* (2), 222-231.
6. Ufimtsev, I. S.; Martinez, T. J., Quantum Chemistry on Graphical Processing Units. 2. Direct Self-Consistent-Field Implementation. *J. Chem. Theory Comput.* **2009,** *5* (4), 1004-1015.
7. Ufimtsev, I. S.; Martinez, T. J., Quantum Chemistry on Graphical Processing Units. 3. Analytical Energy Gradients, Geometry Optimization, and First Principles Molecular Dynamics. *J. Chem. Theory Comput.* **2009,** *5* (10), 2619-2628.
8. Seritan, S.; Bannwarth, C.; Fales, B. S.; Hohenstein, E. G.; Isborn, C. M.; Kokkila-Schumacher, S. I. L.; Li, X.; Liu, F.; Luehr, N.; Snyder Jr, J. W.; Song, C.; Titov, A. V.; Ufimtsev, I. S.; Wang, L.-P.; Martínez, T. J., TeraChem: A graphical processing unit-accelerated electronic structure package for large-scale ab initio molecular dynamics. *WIREs Comput. Mol. Sci* **2021,** *11* (2), e1494.
9. Ong, M. T.; Leiding, J.; Tao, H.; Virshup, A. M.; Martínez, T. J., First Principles Dynamics and Minimum Energy Pathways for Mechanochemical Ring Opening of Cyclobutene. *J. Am. Chem. Soc.* **2009,** *131* (18), 6377-6379.
10. Grimme, S.; Antony, J.; Ehrlich, S.; Krieg, H., A consistent and accurate ab initio parametrization of density functional dispersion correction (DFT-D) for the 94 elements H-Pu. *J. Chem. Phys.* **2010,** *132* (15), 154104.
11. Kästner, J.; Carr, J. M.; Keal, T. W.; Thiel, W.; Wander, A.; Sherwood, P., DL-FIND: An Open-Source Geometry Optimizer for Atomistic Simulations. *J. Phys. Chem. A* **2009,** *113* (43), 11856-11865.
12. Metz, S.; Kästner, J.; Sokol, A. A.; Keal, T. W.; Sherwood, P., ChemShell—a modular software package for QM/MM simulations. *WIREs Comput. Mol. Sci* **2014,** *4* (2), 101-110.
13. Henkelman, G.; Jónsson, H., A dimer method for finding saddle points on high dimensional potential surfaces using only first derivatives. *J. Chem. Phys.* **1999,** *111* (15), 7010-7022.
14. Kästner, J.; Sherwood, P., Superlinearly converging dimer method for transition state search. *J. Chem. Phys.* **2008,** *128* (1), 014106.
15. Fukui, K., The path of chemical reactions - the IRC approach. *Acc. Chem. Res.* **1981,** *14* (12), 363-368.
16. Eyring, H., The Activated Complex in Chemical Reactions. *J. Chem. Phys.* **1935,** *3* (2), 107-115.
17. Evans, M. G.; Polanyi, M., Some applications of the transition state method to the calculation of reaction velocities, especially in solution. *Trans. Faraday Soc.* **1935,** *31* (0), 875-894.
18. Wigner, E., The transition state method. *Trans. Faraday Soc.* **1938,** *34* (0), 29-41.
19. Frisch, M. J.; Trucks, G. W.; Schlegel, H. B.; Scuseria, G. E.; Robb, M. A.; Cheeseman, J. R.; Scalmani, G.; Barone, V.; Petersson, G. A.; Nakatsuji, H.; Li, X.; Caricato, M.; Marenich, A. V.; Bloino, J.; Janesko, B. G.; Gomperts, R.; Mennucci, B.; Hratchian, H. P.; Ortiz, J. V.; Izmaylov, A. F.; Sonnenberg, J. L.; Williams; Ding, F.; Lipparini, F.; Egidi, F.; Goings, J.; Peng, B.; Petrone, A.; Henderson, T.; Ranasinghe, D.; Zakrzewski, V. G.; Gao, J.; Rega, N.; Zheng, G.; Liang, W.; Hada, M.; Ehara, M.; Toyota, K.; Fukuda, R.; Hasegawa, J.; Ishida, M.; Nakajima, T.; Honda, Y.; Kitao, O.; Nakai, H.; Vreven, T.; Throssell, K.; Montgomery Jr., J. A.; Peralta, J. E.; Ogliaro, F.; Bearpark, M. J.; Heyd, J. J.; Brothers, E. N.; Kudin, K. N.; Staroverov, V. N.; Keith, T. A.; Kobayashi, R.; Normand, J.; Raghavachari, K.; Rendell, A. P.; Burant, J. C.; Iyengar, S. S.; Tomasi, J.; Cossi, M.;

Millam, J. M.; Klene, M.; Adamo, C.; Cammi, R.; Ochterski, J. W.; Martin, R. L.; Morokuma, K.; Farkas, O.; Foresman, J. B.; Fox, D. J. *Gaussian 16 Rev. C.01*, Wallingford, CT, 2016.
20. Wheeler, S. E.; Houk, K. N.; Schleyer, P. v. R.; Allen, W. D., A Hierarchy of Homodesmotic Reactions for Thermochemistry. *J. Am. Chem. Soc.* **2009,** *131* (7), 2547-2560.